THESIS

FORMATION OF RAIN LAYERS IN THE INDIAN OCEAN AND THEIR FEEDBACKS TO ATMOSPHERIC CONVECTION

Submitted by

Kyle T. Shackelford

Department of Atmospheric Science

In partial fulfillment of the requirements

For the Degree of Master of Science

Colorado State University

Fort Collins, Colorado

Spring 2023

Master's Committee:

Advisor: Peter Jan van Leeuwen
Co-Advisor: Charlotte DeMott

Eric Maloney
Karan Venayagamoorthy

ABSTRACT

FORMATION OF RAIN LAYERS IN THE INDIAN OCEAN AND THEIR FEEDBACKS TO ATMOSPHERIC CONVECTION

Rainfall over the tropical warm pool spanning the Indian and West Pacific Oceans is relatively colder, fresher, and less dense than the near-surface ocean. Thus, under low-to-moderate winds, rainfall can act to stably stratify the upper ocean, forming a rain layer (RL). RLs cool and freshen the ocean surface and shoal ocean mixed layer depth, confining air-sea interaction to a thin, near-surface ocean layer. The shallow, transient nature of RLs has limited their observation, and RL impact on air-sea interaction is not well understood. This two-part thesis aims to address knowledge gaps surrounding 1) RL formation and characteristic traits, and 2) RL feedbacks to the atmosphere.

In the first part of this thesis, we examine Indian Ocean RLs and their potential feedbacks to the atmosphere using a 1D ocean model. Initial experiments focus on model validation, and demonstrate that the model is able to effectively replicate upper ocean response to precipitation as revealed by in situ measurements. Following model validation, Indian Ocean RL characteristics are studied by forcing a 2D array of 1D model columns with atmospheric output from an existing convection-permitting simulation. Results from this experiment demonstrate that SST reduction within RLs persists on time scales longer than those of the parent rain event. To evaluate RL feedbacks to the atmosphere, a second 2D array experiment is conducted over the same domain with identical atmospheric forcing except rainfall is set to zero at every time step. Comparison between simulations with and without rain forcing demonstrate that RLs reduce SST through cold rain input to the ocean surface, and maintain and enhance SST reductions through a stable salinity stratification. Through prolonged SST reduction, RLs also enhance spatial SST gradients that have previously been shown to excite atmospheric convection.

In the second part of this thesis, RL feedbacks to the Madden-Julian Oscillation (MJO) are studied by conducting regional ocean-atmosphere coupled simulations. Output from two convection-permitting coupled simulations of the November 2011 MJO event, one with rain coupling to the ocean surface and a second without rain coupling, is used to evaluate two potential RL feedback mechanisms. The first feedback is the “SST gradient effect,” which refers to RL-enhanced SST gradients imposing low-level

patterns of convergence/divergence in the atmospheric boundary layer. The second is the "SST effect," which refers to RL-induced SST perturbations altering turbulent heat fluxes. During the MJO transition from suppressed to enhanced convection, the SST gradient effect and SST effect have opposing feedbacks to convection, as RL-enhanced SST gradients favor convective initiation, while RL-induced SST reduction hinders convection. Comparison of coupled simulations with and without rain coupling to the ocean demonstrates that RL-induced SST reduction has a more substantial impact than enhanced SST gradients during this transitory phase. A delayed pathway in which RLs feedback to the MJO through the SST effect arises from frequent RL presence during the disturbed phase, which isolates subsurface ocean heat from the atmosphere. At the onset of the MJO active phase, westerly wind bursts erode near-surface RLs and release previously trapped subsurface ocean heat to the atmosphere, amplifying the intensity of MJO convection. Between the direct and delayed SST effect, RLs are shown to modify intraseasonal tropical variability.

TABLE OF CONTENTS

LIST OF TABLES

LIST OF FIGURES

CHAPTER 1

INTRODUCTION

The Madden-Julian Oscillation (MJO) is a planetary-scale convective disturbance that represents the dominant mode of intraseasonal tropical variability (Madden and Julian (1971)). Over the tropical warm pool, the MJO can be identified through eastward moving regions of enhanced and suppressed cloudiness. MJO influence on weather and climate extends spatially beyond the tropics through Rossby waves excited by MJO-induced diabatic heating anomalies that propagate poleward and influence extratropical circulation (Hoskins and Karoly (1981); Weickmann (1983)). Furthermore, despite it's 30 to 60 day period, MJO influence on global climate extends temporally to interannual time scales through modification of El Niño Southern Oscillation (ENSO) events (McPhaden et al. (1988)). While the MJO is considered to be primarily atmospherically-driven, improved MJO representation in ocean-atmosphere coupled simulations compared to uncoupled simulations suggests the ocean also modifies MJO timing and intensity (e.g., DeMott et al., 2019; Kemball-Cook et al., 2002; Zhang et al., 2006). However, the role of the ocean in regulating MJO convection is not fully understood.

The ocean feeds back to MJO convection through SST perturbations that are regulated by upper ocean stability. Solar heating of the ocean under the MJO region of suppressed cloudiness stabilizes the upper ocean during the day, forming stable diurnal warm layers (DWLs; e.g., Bellenger & Duvel (2009); Soloviev et al. (1997)). DWLs support anomalous high SST, which in turn enhances surface turbulent heat flux into the atmosphere and moistens the free troposphere ahead of MJO convection (de Szoeke and Maloney (2020); DeMott et al. (2016); Ruppert Jr. and Johnson (2016); Zhang and Anderson (2003)). As the MJO transitions from suppressed to enhanced cloudiness, increasing rainfall can act to stabilize the upper ocean through input of fresher, colder, less dense rainwater on the ocean surface, forming rain layers (RLs; e.g., Drushka et al. (2016); Reverdin et al. (2012); Asher et al. (2014)). RLs also have potential to influence MJO convection, but understanding of RL feedbacks to convection remains unclear. Locally, RLs reduce SST which inhibits deep convection, however, RLs may also enhance spatial SST gradients that support convective initiation (Back and Bretherton (2009a); Li and Carbone (2012); Lindzen and Nigam (1987)). While DWLs have been widely observed due to their broad spatial footprint and regular temporal nature, the transient, irregular nature of precipitation has limited RL observation. These observational constraints have limited understanding RL characteristics and potential RL feedbacks to the MJO during the suppressed to enhanced transition.

Idealized modeling experiments (Drushka et al. (2016); Iyer and Drushka (2021a)) and single-point observational analyses (Asher et al. (2014); Drushka et al. (2019b); Iyer and Drushka (2021b); Thompson et al. (2019)) form the basis of current understanding of RL characteristics. While these studies have contextualized ocean response to precipitation in terms of atmospheric forcing and ocean state, idealized experiments provide limited information about RL behavior under realistic atmospheric conditions, and ship-based observations are expensive to collect and limited to a single point. We target these knowledge gaps in RL behavior by forcing a 2D array of 1D ocean columns using realistic atmospheric forcing from an existing convection-permitting simulation. Output from this simulation is used to develop statistics describing RL lifetime, frequency, spatial footprint, and stratification. These experiments also demonstrate that RLs have the potential to influence the atmosphere by enhancing SST cooling following rainfall and generating small-scale SST gradients. Results from these simulations are found in chapter 2, and are also published in *Journal of Geophysical Research: Oceans* as,

- Shackelford, K., DeMott, C. A., van Leeuwen, P. J., Thompson, E., & Hagos, S. (202s). Rain-induced Stratification of the Equatorial Indian Ocean and Its Potential Feedback to the Atmosphere. *Journal of Geophysical Research: Oceans*, 127(3), e2021JC018025.

Results from chapter 2 suggest RLs have the potential to feedback to the atmosphere through RL-induced SST perturbations and RL enhancement of spatial SST gradients. However, the experiments in chapter 2 are uncoupled and provide no description of atmospheric response to RL-induced changes to the SST field. Thus, to evaluate RL influence on the atmosphere through SST perturbations and enhanced SST gradients we conduct regional ocean-atmosphere coupled simulations over the tropical Indian Ocean. The role of RLs in regulating MJO convection is investigating by conducting experiments with and without rain coupling to the ocean surface. Qualitative and quantitative comparisons between these experiments suggests that RL-induced SST perturbations have a more substantial influence on atmospheric convection than RL enhancement of SST gradients. Furthermore, SST perturbations in RLs are shown to influence the MJO through direct and delayed pathways that arise from distinct physical mechanisms. Results from these simulations are found in chapter 3, and will also be submitted for publication to *Journal of Geophysical Research: Atmospheres*.

Chapter 4 offers a succinct summary of our results, as well as a discussion on the future implications of this work.

CHAPTER 2

RAIN-INDUCED STRATIFICATION OF THE EQUATORIAL INDIAN OCEAN AND ITS POTENTIAL FEEDBACK TO THE ATMOSPHERE

2.1 INTRODUCTION

Upper ocean stratification is the result of processes that form or advect low-density water layers on top of higher-density water layers. Stratification is affected by many processes, including upwelling, wind stirring, warming from solar radiation, salinification due to evaporation, and surface freshening from precipitation and river run-off (Asher et al. (2014); Bellenger and Duvel (2009); Drushka et al. (2016); Hughes et al. (2020); Kraus and Turner (1967); Soloviev and Lukas (1997); Thompson et al. (2019)). Ocean stratification regulates vertical mixing of heat, nutrients, and gases, and affects climatologically important low-frequency ocean processes, such as the formation of North Atlantic deep water (Broecker (1991)), carbon uptake (Watson et al. (2020)), and the El Niño–sthern Oscillation (Cronin and McPhadden (2002)).

On shorter timescales, near-surface stable layers induced by the diurnal cycle of surface solar heating are classified as diurnal warm layers (DWLs) while those induced by freshwater fluxes from rainfall are classified as rain layers (RLs), or fresh water lenses. Stabilization within RLs and DWLs shoals (i.e., makes more shallow) the ocean mixed layer and reduces vertical mixing between the near-surface ocean and the ocean mixed-layer by altering upper ocean temperature and salinity profiles. Through their ability to resist vertical mixing, these shallow stable layers may then confine subsequent surface inputs of heat, momentum, and freshwater to the upper 1 to 10 m of the ocean. Changes to sea surface temperature (SST) and sea surface salinity (SSS) within these near-surface stable layers modify fluxes of heat, moisture, and momentum across the air-sea interface.

The spatially broad and temporally regular nature of DWLs has allowed for extensive study of these phenomena, and their impact upon atmospheric convection is well-documented (Bellenger and Duvel (2009); Bellenger et al. (2010); de Szoeke et al. (2021)). Increased SST within DWLs deepens the atmospheric boundary layer and helps regulate the diurnal cycle of convection in the tropics, and inclusion of DWL parameterizations in atmospheric models has improved forecasting of the MJO (Woolnough et al. (2007); Zhao and Nasuno (2020)) and ENSO (S. et al. (2012); Terray et al. (2012)), indicating that DWLs contribute to climate variability on the intraseasonal and interannual timescales. However, while DWLs are the result of diurnal surface heating that is often quasi-uniform over large scales, RLs

are the result of intermittent precipitation which can be highly irregular for a given location. As such, less is known about the spatiotemporal characteristics of RLs or their cumulative effects on the atmosphere.

While multiple studies record changes to upper ocean profiles within DWLs (Bellenger and Duvel (2009); Fairall et al. (1996b); Hughes et al. (2020); Soloviev and Lukas (1997); Stuart-Menteth et al. (2003)), knowledge of how RLs adjust upper ocean salinity and temperature profiles, as well as air-sea exchange, has been limited by observational constraints. Currently, operational satellites tasked with measuring SSS include the Soil Moisture, Active/Passive (SMAP; Vinogradova et al., 2019), with a 40km footprint and 2-3 day revisit time, and the Soil Moisture Ocean Salinity (SMOS; Vinogradova et al., 2019), with a 43km footprint and 3-5 day revisit time, which are too infrequent and spatially coarse to capture the impacts of convective scale to mesoscale surface freshening (DeMott and Rutledge (1998); Richenback and Rutledge (1998)). Moorings provide nearly continuous observations at coarse horizontal resolution, but their coarse vertical resolution of the upper ocean prevents investigation of the near-surface impacts of RLs. Similarly, operational Argo floats are usually limited by coarse upper ocean vertical resolution, as well as coarse horizontal and temporal sampling (Gould et al. (2004)). The most useful observations for investigating RLs have been provided by field campaigns, which allow for ship-based, collocated ocean-atmosphere observations, with frequent sampling and fine-scale vertical resolution. However, field campaigns are held infrequently and for limited duration, thus limiting the direct observation of changes to SSS, SST, and surface fluxes within RLs.

Thompson et al. (2019) used upper ocean observations collected in the equatorial Indian Ocean as part of the Dynamics of the Madden-Julian Oscillation field campaign (DYNAMO; Yoneyama et al, 2013) to study near-surface stabilization in DWLs and RLs. They found that while the freshening and cooling of the upper ocean have opposing effects on stability, the positive buoyancy produced by freshening is generally about an order of magnitude greater than the negative buoyancy produced by cooling. Additionally, they observed that RL-induced buoyancy is strong enough to withstand nocturnal ocean convective mixing and wind-driven mixing for wind speeds up to 9.8 m s^{-1} for the heaviest rain rates. Mean RL lifetime observed by Thompson et al. (2019) was 5 hours, with some RLs lasting nearly a full day. Thus, the typical RL lifetime is longer than the typical lifetime of rain events that initiate RLs (Hagos et al. (2013)).

RL persistence on the scale of hours suggests that RL lifetimes are long enough to impact the atmospheric boundary layer (de Szoeke et al. (2017); DeMott et al. (2015)), but RL feedback to atmospheric

convection is not straight-forward. Locally, RLs stabilize and cool the upper ocean, potentially hindering the initiation of new convection (Ruppert Jr. and Johnson (2016)) and reducing the maintenance of existing convection by surface fluxes (Riley Dellaripa and Maloney (2015)). However, sharp SST gradients exist between the RL and surrounding ocean, generating horizontal pressure gradients that act to initiate boundary layer convergence and stimulate atmospheric convection (Back and Bretherton (2009a,b); Li and Carbone (2012); Rydbeck et al. (2019); Skyllingstad et al. (2019)). The nature of the atmospheric response to RL formation remains an important open question for understanding the impact of of freshwater ocean surface stratification on atmospheric convection.

Recently, idealized model experiments have increased understanding of RL characteristics, revealing the importance of rain rate, wind speed, and background ocean stratification in regulating RL behavior (Drushka et al. (2016); Iyer and Drushka (2021a); Soloviev et al. (2015)). While experiments investigating RLs in an idealized environment have provided insight into upper ocean response to precipitation, the collective effects of RLs under realistic, time-varying atmospheric forcing on SST patterns, surface fluxes, and feedbacks to atmospheric convection is less understood. We aim to address this knowledge gap with a modeling study designed to answer the following science questions:

(1) What is the size, frequency, duration, and intensity of equatorial Indian Ocean RLs on monthly time scales?

(2) To what extent do RLs alter surface fluxes and create small-scale networks of SST gradients?

To address these questions, a 1-dimensional water column model is used to simulate freshwater stratification in the equatorial Indian Ocean. The design of the model simulations is discussed in section 2. The model is first verified when forced with surface observations collected during DYNAMO and compared to observed ocean stability profiles. Results from this analysis are shown in section 3. After model verification, a 50 km x 50 km 2D array of 1D columns is forced with surface meteorology at 2 km resolution from an existing simulation of the regional atmospheric Weather Research and Forecasting model (WRF; Skamaock et al. 2019). Stratification by surface freshening is analyzed to determine spatial and temporal characteristics of RLs that result from the multitude of spatially and temporally inhomogeneous, model-simulated rain and wind events. We present results from this analysis in sections 4 and 5, and further discuss the implications of these results in section 6. In section 7, we conclude with a brief summary that highlights the primary conclusions of this study.

2.2 METHODS

In this section, the General Ocean Turbulence Model (GOTM) is introduced (section 2.1). The specifics of two model simulations are discussed, where the first simulation serves the purpose of model verification (2.2), while the second is used to generate statistics describing RL characteristics and variability of upper ocean stability (2.3, 2.4).

2.2.1 Model Configuration

GOTM is a water-column model that computes solutions for the one-dimensional version of the transport equations of momentum, salt, and heat (Burchard et al. (1999)). The version of GOTM implemented in this study closely follows the model setup of Drushka et al. (2016), which has been shown to effectively replicate upper ocean temperature and salinity response to rainfall. This version of GOTM utilizes a second-order turbulence closure scheme (Canuto et al. (2001)) with dynamic dissipation rate equations for the length scales. Fluxes are calculated following the Coupled Ocean-Atmosphere Response Experiment (COARE) bulk flux algorithm (Fairall et al. (1996)), which uses skin temperature to compute surface fluxes. Longwave radiation is calculated following Clark (1974). GOTM assumes wet bulb temperature for rainfall, which is supported by observations (Gosnell et al. (1995)). The model is run with a 10-second time step and initialized to a depth of 70 meters with 10-centimeter vertical resolution. GOTM's sensitivity to upper ocean vertical resolution was tested at vertical resolutions of 1 cm, 10 cm, 50 cm and 100 cm, and negligible improvement was seen in model performance at vertical resolution below 10 cm. GOTM receives surface forcing input in the form of horizontal components of the 10-meter winds, and surface values of air temperature, air pressure, relative humidity, incident shortwave radiation, and rain rate. In this study, GOTM is forced first using observations collected during the DYNAMO field campaign (Gottschalck et al. (2013); Yoneyama et al. (2013)), and then using Weather Research and Forecasting (WRF) model output from a 2014 study by Hagos et al. The details of the surface forcing data are outlined in the following sections.

2.2.2 Model verification and DYNAMO data

The DYNAMO field campaign was conducted in the Indian Ocean from October 2011 through March 2012, with the purpose of observing convective initiation processes associated with the MJO. The field campaign was an international effort featuring two quadrilateral sounding arrays, multiple radars, simultaneous and continuous observations of atmospheric and oceanic profiles conducted from three moorings and two ships (research vessel (R/V) Roger Revelle and R/V Mirai), twin sites in the Indian Ocean (Addu Atoll) and Western Pacific (Manus Island) to sample the MJO at its initiation,

mature, and dissipating phases, and an aircraft operation for sampling atmospheric and oceanic coupled boundary layers (Chen et al. (2016); Yoneyama et al. (2013)).

Of interest for this study are the high-frequency atmospheric and oceanic observations collected from the R/V Revelle (80.5°E, 0°N) during the October 5 through October 30 and November 11 through December 7, 2011 DYNAMO observing periods. Each period sampled one full MJO event (Gottschalck et al. (2013)), and thus featured a broad spectrum of ocean-atmospheric variability, from strongly suppressed and light-rain conditions to highly disturbed and heavy-rain conditions. The observations from the R/V Revelle are unique in that they feature collocated ocean-atmosphere observations that are high-resolution both temporally (upper ocean profiles observed at roughly 7-minute intervals), and vertically (1-meter resolution for upper ocean observations) (Moum et al. (2014)). The fine vertical resolution of the upper ocean observations, which begin at a depth of 2-3 m (Thompson et al. (2019)), allows for detailed comparisons of GOTM output to observations made from the R/V Revelle. Additionally, the frequent nature of the observations allows for transient rain events to be effectively captured within both meteorological surface data and near-surface ocean temperature and salinity profiles. Thompson et al. (2019) analyzed these same observations to study RLs and DWLs.

For the first DYNAMO simulation, GOTM is initialized with temperature and salinity profiles from the R/V Revelle on 6 October 2011 at 01:30:00 UTC, and is then forced with atmospheric observations at 10-minute intervals until 12:00:00 UTC on 30 October. For the second DYNAMO simulation, GOTM is initialized with temperature and salinity profiles from the R/V Revelle on 11 November 2011 19:20:00 UTC and is again forced with atmospheric observations at 10-minute intervals until 8 December 2011 05:30:00 UTC. No relaxation to an observed or climatological mean temperature and salinity profile was needed to replicate the observed upper ocean conditions. Each simulation captures observed intraseasonal variability attributable to the MJO, with conditions varying from fair weather with low cloudiness, light rainfall, calm winds, and high incident shortwave radiation during the MJO suppressed phase to deep and widespread cloudiness, heavy precipitation, strong winds, and reduced surface solar radiation during the MJO disturbed phase, enabling comparison of GOTM model output to observations under diverse conditions

For each DYNAMO simulation, GOTM stability profiles are calculated using vertical gradients in potential density to find the Brünt-Vaisala frequency, N^2:

$$N^2 = \frac{g}{\sigma}\frac{d\sigma}{dz} \tag{2.1}$$

As salinity and temperature both play important roles in ocean stratification, upper ocean stability as indicated by N^2 is governed by vertical gradients of both quantities. To view temperature (T) and salinity (S) contributions to N^2 separately, N^2 can be decomposed into its temperature and salinity components, N_T^2 and N_S^2, defined as :

$$N_T^2 = g \cdot \alpha \cdot \frac{dT}{dz} \tag{2.2}$$

$$N_S^2 = g \cdot \beta \cdot \frac{dS}{dz} \tag{2.3}$$

where β is the haline contraction coefficient of seawater, and α is the thermal expansion coefficient of seawater:

$$\beta = \frac{1}{\sigma}\frac{d\sigma}{dS} \tag{2.4}$$

$$\alpha = \frac{-1}{\sigma}\frac{d\sigma}{dT} \tag{2.5}$$

This decomposition allows for identification of RLs, which are present when the upper ocean is stably stratified with respect to both total N^2 and it's salinity component, N_S^2, and DWLs, which are present when the upper ocean is stably stratified with respect to both total N^2 and it's temperature component, N_T^2. Following the methods of Thompson et al. (2019), the column is considered to be stable if $N^2 > 4.5\times10^{-5}$ s^{-1} for two consecutive vertical layers; otherwise, the column is considered well-mixed. Modeled N^2 values are computed every 0.5 m for the upper 20 meters of the ocean; thus, minimum thickness for a layer to be considered stable is 1 m. For both observational and model analysis, the upper ocean is considered well-mixed if no stable layers are identified in the upper 20 m of the ocean. Observations synthesized by Thompson et al. (2019) were used to validate model output. Since observations are collected with a vertical resolution of 1-meter, the column is considered stable for two consecutive 1-meter layers and minimum thickness of observed stable layers is 2 meters, compared to a minimum thickness of 1 meter for modeled stable layers.

2.2.3 WRF data and GOTM 2D array

For the second portion of this study, a 2D array of GOTM columns is forced with model output from a WRF simulation conducted by Hagos et al. (2014). WRF was run at 2 km horizontal resolution over a $3^\circ \times 3^\circ$ latitude-longitude area within the Indian Ocean DYNAMO domain from 1 October 2011 to 30 November 2011. This grid spacing is fine enough to resolve individual convective systems while the domain is large enough and the simulation long enough to capture lifecycles of convective systems associated with synoptic scale features (Chen et al. (1996); Hagos et al. (2014)) This makes the WRF data well-suited for this study: the 2 km grid spacing resolves atmospheric convective-scale forcing of

the upper ocean, while the spatial domain allows for the development of organized mesoscale convective systems that contribute to the variability of surface forcing. Surface boundary conditions in the WRF simulation are provided by ERA-Interim reanalysis, and applied at 6-hour intervals. Comparison between WRF precipitation output and TRMM satellite observations shows that while WRF is able to capture the overall eastward propagation of the two MJO events during October and November 2011, the model precipitation tends to be higher than TRMM observations. Hagos et al. (2014) attribute this discrepancy to the model resolution, which limits turbulent mixing and evaporation of rain. Further details on the WRF parameterizations can be found in Hagos et al. (2014).

An initialized model, the specifications of which are discussed in the next section, was trained with the mined data from the ELDORA dataset. The X and Y arrays from the data collection stage were split at random with 80% and 20% reserved for training and testing respectively. Initial splitting of the data before training ensures the model has not previously encountered the testing set. The trained model classified all radar gates in the X testing array to create a new set of classifications. Predicted classes were compared to the true classifications in the Y testing array. Evaluation metrics were produced to assess how well the model retained and removed weather and non-weather echoes.

To investigate spatiotemporal variability of RLs, the 2D array of GOTM columns is forced with output from the WRF simulation over a 50 km × 50 km grid, centered over 75°E, 0°N with 2 km grid spacing. This 50 km × 50 km domain allows investigation of fine-scale spatial variability of upper ocean temperature and salinity profiles, sea-surface temperature (SST), and sea-surface salinity (SSS) on scales smaller than those currently resolved by most global models and satellite-estimated SSS products. Initial conditions for the temperature and salinity profile at each grid cell are obtained from the Hybrid Coordinate Ocean Model (HYCOM) reanalysis dataset (Chassignet et al. (2007)). HYCOM provides vertical temperature and salinity at depths of 0.05 m, 2 m, 4 m, 6 m, 8 m, 10 m, 12 m, 15 m, 20 m, 25 m, 30 m, 35 m, 40 m, 45 m, 50 m, 60 m, 70 m, which are then linearly interpolated by GOTM to a 10-cm grid spacing from 0-70 meters. The more coarse horizontal grid spacing in the HYCOM reanalysis (0.08°) is linearly interpolated to the WRF grid. Analysis of the DYNAMO simulations shows GOTM sensitivity to small variations in initial temperature and salinity profiles to be small compared to variations introduced via surface forcing. The 2D array simulation is run from 00 UTC 1 November 2011 to 18 UTC 30 November 2011. GOTM is again forced at 10-minute intervals with no relaxation to a reference temperature or salinity profile.

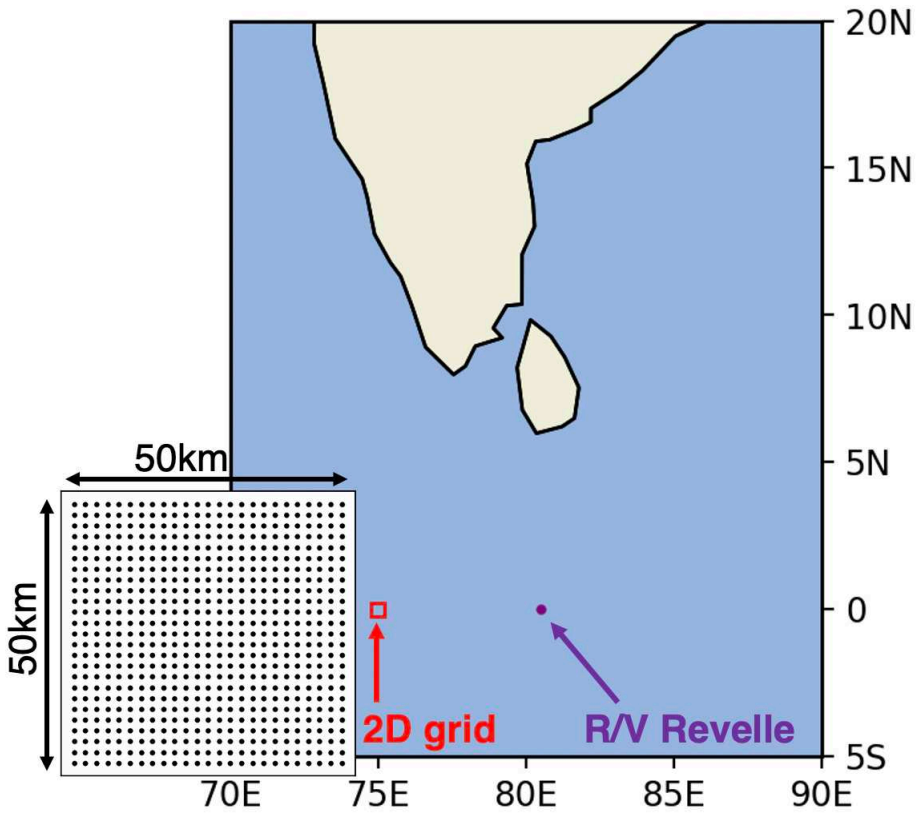

FIG. 2.1. Model domain for the two GOTM simulations: the location of the R/V Revelle during DYNAMO (purple) and domain for the 2D array experiment (red box). The inset grid displays the dimensions and layout of the 2D array.

We use GOTM output from the 2D array simulation to conduct a statistical analysis detailing RL characteristics. The 2D domain allows for analysis of RL characteristics under spatially variable wind and rain forcing over a typical MJO lifecycle, for a satellite footprint-sized domain. To conduct this analysis, we first use the stable layer identification algorithm described in Section 2.2 to detect rain layers. We then investigate RL behavior as function of rain rate, wind speed, and background ocean stratification (section 4.1). In section 4.2 we make approximations of RL size as determined by RL equivalent diameter and in section 4.3 we analyze reduced mixing in RLs using the temperature tendency equation in GOTM. Finally, we examine the potential for RLs to influence the atmospheric boundary layer by repeating the second simulation over the 2D domain without rain forcing (i.e., rain rate, R,=0 everywhere, for all time steps) but with all other atmospheric forcing fields identical (section 5).

2.3 Model verification: comparisons to DYNAMO observations

While previous studies have verified the ability of GOTM to simulate observed upper ocean response to precipitation (Drushka et al. (2016)), upper ocean observations from the R/V Revelle allow for a more detailed comparison of stable layers analyzed by Thompson et al. (2019) to those simulated by GOTM. Furthermore, the October and November DYNAMO legs provide an opportunity to evaluate GOTM performance under different background conditions, as an advection event brought high salinity water from the Arabian Sea into the DYNAMO domain between the October and November observing periods. The high-salinity water mass contributed to the formation of a barrier layer that was present throughout the November observation period.

Initial steps in model verification involve comparison of GOTM temperature and salinity profiles to profiles observed during the October and November DYNAMO legs. Time series comparison between GOTM SST and observed SST for both simulations confirms that the model effectively replicates the strong diurnal cycle of SST during suppressed MJO conditions, as well as the reduced, diurnally uniform SST during active MJO conditions and westerly wind burst (WWB) events (Figure 2.2). Modeled SST mean absolute error for the October and November observing periods is 0.14°C and 0.24°C, respectively.

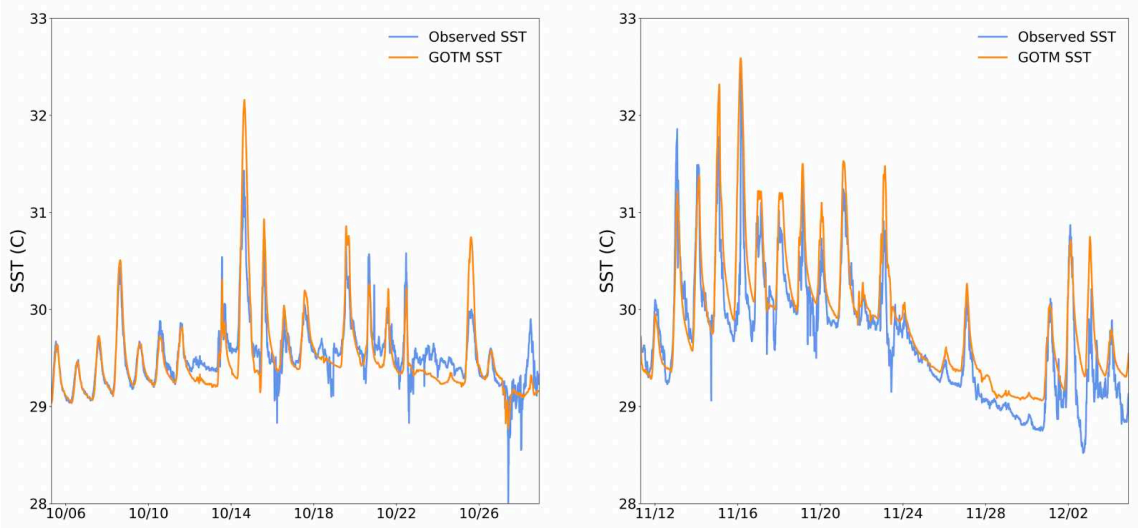

FIG. 2.2. Modeled (orange) and observed (blue) SST time series for the October (left) and November (right) DYNAMO observing periods.

Composite analysis is used to make qualitative comparisons between N^2 profiles computed using model output and observations for the October and November DYNAMO observing periods. For the composite analysis, each 24-hour, 1-day period in the simulation is binned by daytime mean wind

speed in intervals of 2 m s^{-1}, and the mean N^2, N_T^2, and N_S^2 profiles are computed for each wind regime. These composites are then compared to observed N^2, N_T^2, and N_S^2 profiles, i.e., those computed by Thompson et al. (2019) from DYNAMO temperature and salinity observations. Each wind speed interval tends to include multiple days, thus, the composite N^2 profiles are dominated by DWLs and the effects of individual precipitation events are generally not detected. However, this enables a more general evaluation of model performance in capturing changes in vertical stratification as a function of wind speed. Composite N^2 profiles shown in Figure 2.3 demonstrate that GOTM mixing reproduces stratification characteristics of different wind regimes: a persistent, shallow, and strong diurnal signature is present on days with calm winds, a diminished, but deeper, diurnal signature is present on days with moderate winds, and virtually no diurnal signal is detectable on the windiest days, when turbulent mixing is too strong for ocean stratification to develop. Model performance is consistent across the October and November simulations, thus verifying the ability of GOTM to effectively reproduce upper ocean stability profiles under different background ocean stratification. Profiles of N^2 variability computed from GOTM also agree well with those observed during DYNAMO (not shown).

In order to assess model performance in simulation of individual freshening events, a RL detection algorithm is utilized to identify RLs, following criteria outlined in section 2.2 of this paper. It is important to note that salinity observations recorded during DYNAMO begin at a depth of 2-3 m, due to interference from the ship's wake in the upper 2 m of the ocean. Thus, it is useful to evaluate freshening events associated with high precipitation amounts and > 2 m s^{-1} wind speed, as these freshening events generally affect the N_S^2 profile to a depth greater than 2 m. One such case of a RL event with a strong signature below 2 m is found in DYNAMO observations from November 28 when a RL was identified from 02 UTC to 05 UTC. Observed and modeled stability profiles for the November 28 case can be seen in Figure 2.4. The November 28 RL developed following sustained precipitation of > 10 mm hr^{-1}, and during a period of reduced wind speeds (< 10 m s^{-1}) within a longer WWB event, allowing a short-lived RL to form. Figure 2.4 demonstrates that GOTM is able to reproduce the onset, stablization, and duration of the observed RL. November 28 is of further interest as a daily case study due to the sustained precipitation that occurred throughout the day. The high winds present during the day prevented sustained stratification of the upper ocean, but Figure 2.4 reveals multiple brief stratification events in GOTM stability profiles. These highly transient RLs coincide with temporary reductions in wind speed seen throughout the day that allowed for the upper 1-2 m of the ocean to become stably stratified.

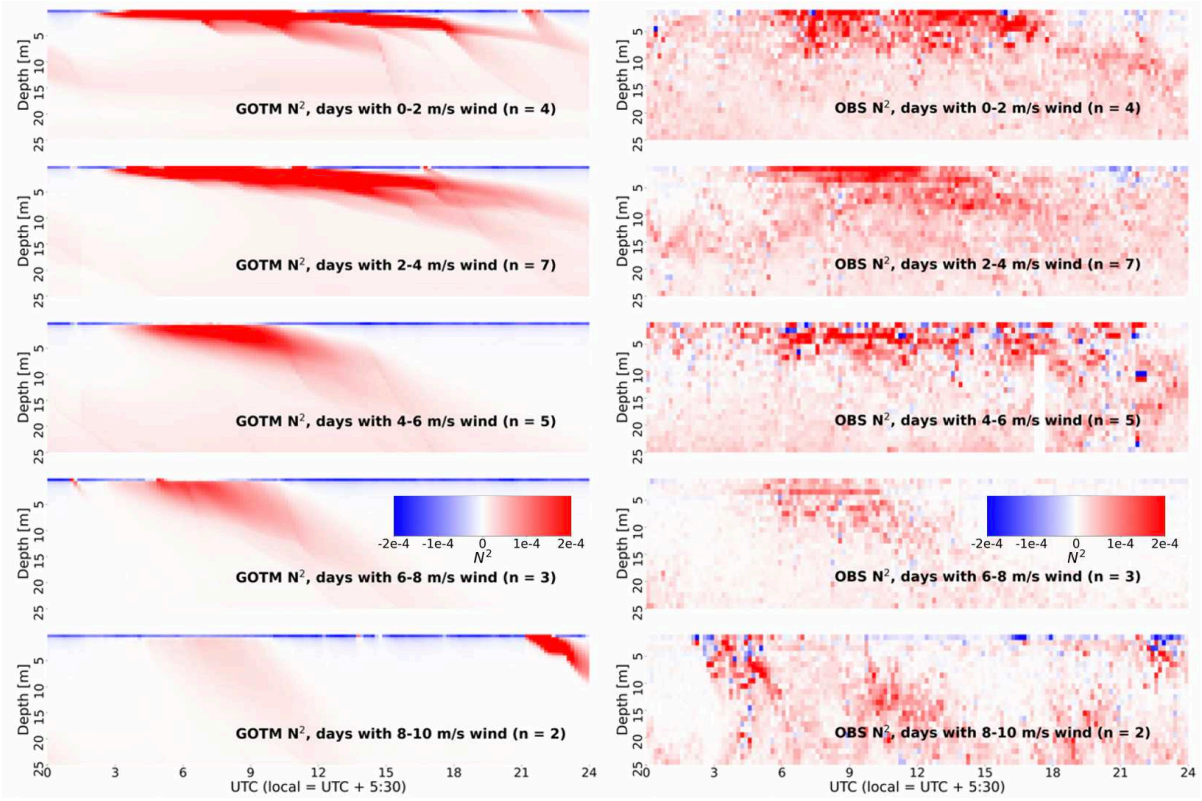

FIG. 2.3. Daily N^2_{T+S} profiles composited by daily wind regime for GOTM (left) and observations (right). Red indicates stable, blue indicates unstable. Number of days within a given wind regime is given by n.

While some of these stratification events are evident in observations, the lack of salinity observations in the upper 2 m inhibits identification of the thinnest RLs.

2.4 RL STATISTICS FROM 2D FORCING EXPERIMENTS

This section applies results from the 2D array simulation to produce statistics defining spatiotemporal characteristics of equatorial Indian Ocean rain layers. The array of GOTM columns is forced at 10-minute intervals with output from a WRF simulation conducted by Hagos et al. (2014; see Section 2.3). We emphasize that these are not ocean-atmosphere coupled simulations. The output from the WRF simulation is simply used to force the 2D GOTM array, and any changes to SST are not communicated to the atmosphere.

For the 2D array simulation, the RL identification algorithm iterates grid cell by grid cell searching the upper 3 m of the ocean for RLs at each time step. Because each GOTM column mixes independently

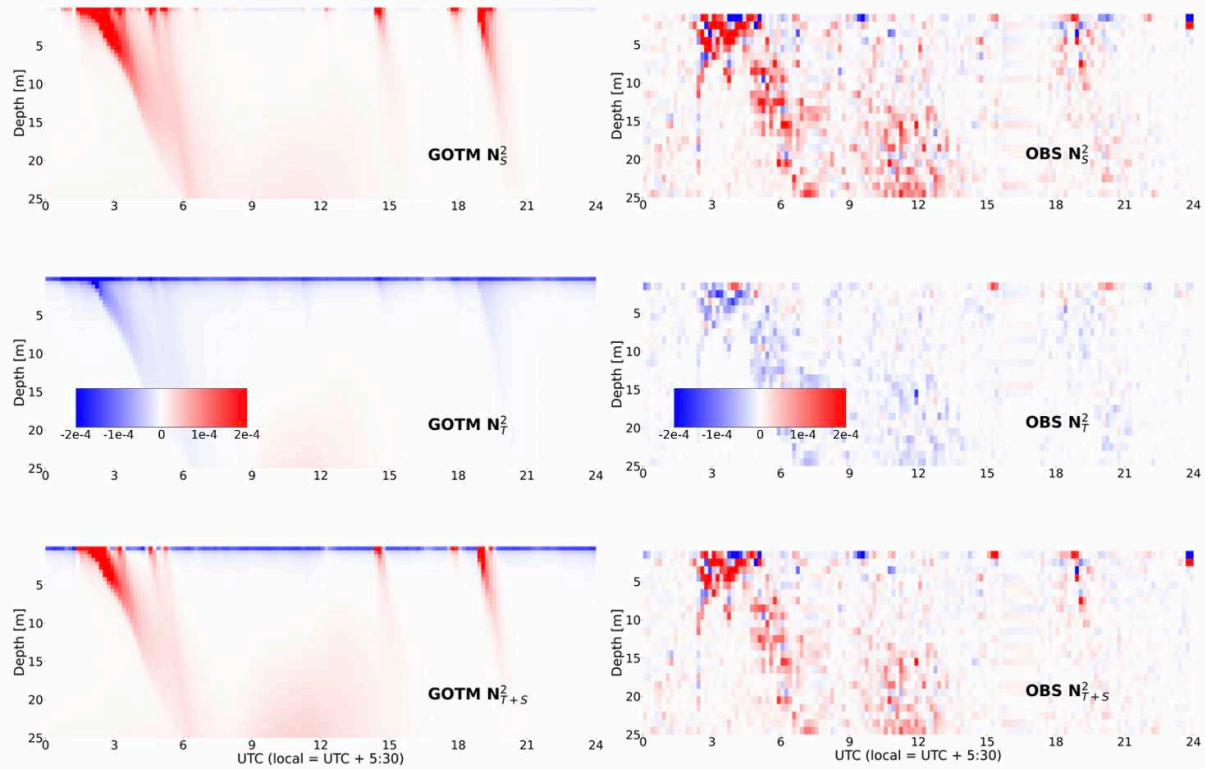

FIG. 2.4. N_S^2 (top), N_T^2 (middle), N_{T+S}^2 (bottom), for 28 November 2011 for GOTM (left) and observations (right). Red indicates stable, blue indicates unstable.

from neighboring columns, we consider each RL-capped column as a separate, distinct RL when computing RL duration, frequency, and intensity statistics (section 4.1). However, we consider adjacent RL-capped columns to be part of a single, larger RL when computing RL size statistics (section 4.2).

2.4.1 RL duration, frequency, and intensity

The duration of RLs over the course of the simulation is highly variable, with modeled RLs persisting on time scales of minutes to days. The distribution of RL lifetime is skewed, as 32% of RLs last less than 30 minutes, 48% last less than 1 hour, and 96% last less than 1 day (Figure 2.5). Mean RL duration is roughly 4.5 hours, which conforms to statistics of RL lifetimes observed during DYNAMO (Thompson et al. (2019)), while median RL duration is just over 1 hour. Although RLs occur at all times, there is a slight increase in RL formation in the early morning and mid-afternoon, which is consistent with the mean diurnal cycle of precipitation over tropical oceans during convectively active and suppressed conditions, respectively (Sui et al. (1997)). Overall, RLs are present in 26% of all model time steps, a higher frequency than the 16% observed by Thompson et al. (2019) during DYNAMO.

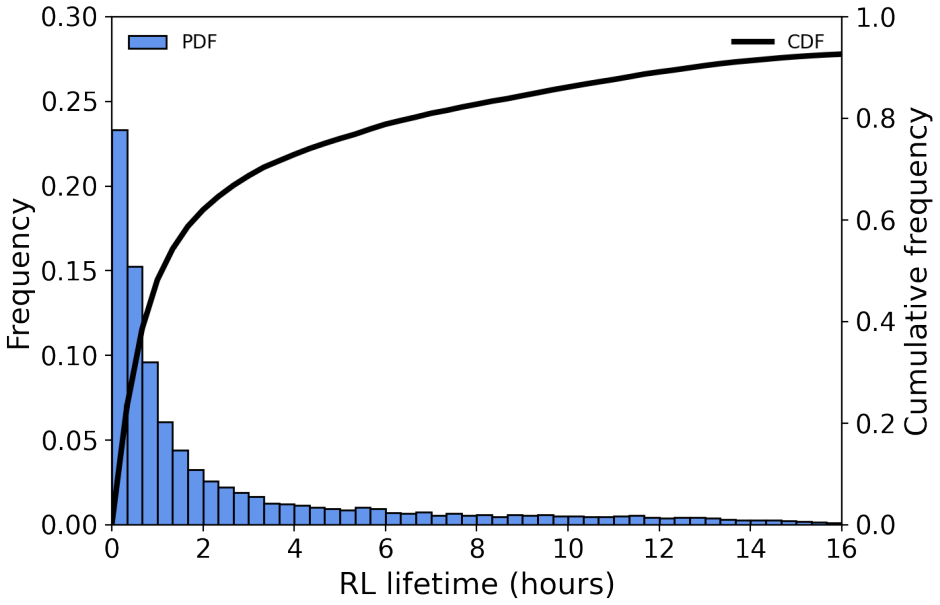

FIG. 2.5. Histogram of RL lifetime frequency, binned by 20-minute intervals (left y-axis), and cumulative frequency (black line; right y-axis)

During periods of low to moderate winds, RLs persist for several hours to over a day, and occur more frequently (Figure 2.6). This is reflected by a RL presence of 32% for time steps when column wind speed is < 5 m s^{-1}, in comparison to a RL presence of 14% for time steps when column wind speed is > 5 m s^{-1}. The 99th percentile wind speed in the presence of RLs is 11.4 m s^{-1}, slightly greater than the 99th percentile wind speed of 9.8 m s^{-1} observed by Thompson et al. However, the 95th percentile wind speed in the presence of RLs is 7.97 m s^{-1}, indicating that rain-induced stratification at wind speeds above 8 m s^{-1} is typically short-lived. When no RLs are present, the 95th percentile wind speed is 10.1 ms^{-1}. The large discrepancy between 95th percentile wind speeds in the presence (7.97 ms^{-1}) and absence (10.1 ms^{-1}) of RLs implies that RLs occur infrequently at wind speeds above 8 m s^{-1}.

Stability profiles of temperature and salinity in the upper ocean are sensitive to wind speed, with the strongest stabilization of both occurring most frequently at wind speeds below 5 m s^{-1}. Histograms of N_S^2 and N_T^2 as a function of wind speed for all model time steps and grid cells are shown in Figure 2.7, and reveal a higher frequency of strong stability in the salinity profile in comparison to the temperature profile. The higher frequency of strong stabilization in the salinity profile is especially evident at higher wind speeds, which is consistent with observational analysis of RLs and DWLs (Thompson et al. (2019)).

Instability can be identified within the temperature profile at wind speeds below 5 ms^{-1} Figure 2.7, a result of both nocturnal convective mixing and unstable temperature profiles within RLs. Composite

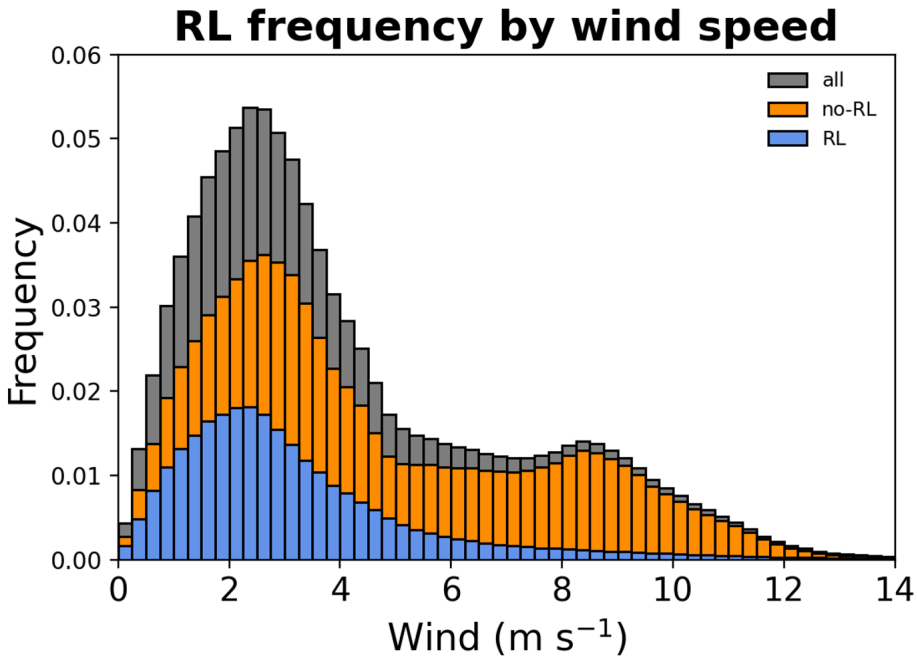

FIG. 2.6. Histogram of wind speed frequency across all GOTM grid cells and times when a RL is present (blue), no-RL is present (orange) and overall (gray)

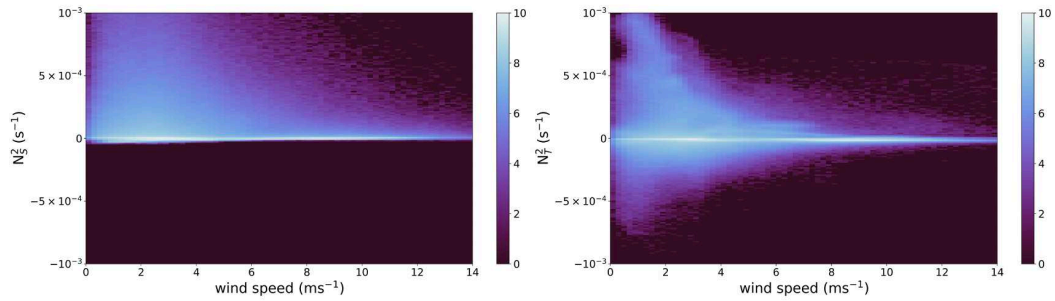

FIG. 2.7. 2D histogram of N_S^2 and wind (left) and N_T^2 and wind (left). Histograms display the natural log value of the count within each bin.

analysis of the N_T^2 response from one hour prior to RL formation to six hours after RL formation as a function of the mean wind speed and maximum rain rate in the ±1 hour interval surrounding RL onset is presented in Figure 2.8 and confirms destabilization in column temperature profiles following RL formation. For RLs forming under background wind speeds < 6 m s^{-1}, unstable temperature gradients confined to the upper 1-2 m persist for many hours following RL formation (Figure 2.8). The persistence of unstable temperature gradients is due to a stronger stabilization of N_S^2, which is also reflected in a net positive N^2 throughout the column (not shown).

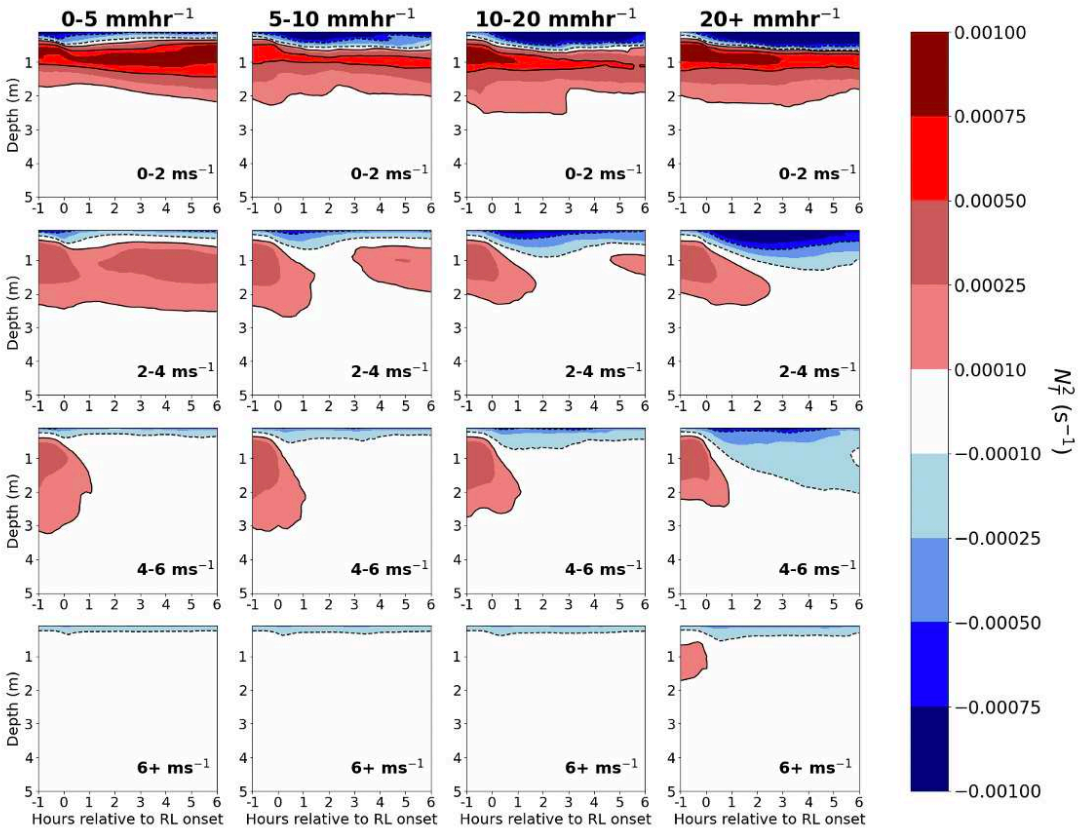

FIG. 2.8. N_T^2 within RLs binned column-wise by max rain rate from 30 minutes prior to 30 minutes after RL formation, and row-wise by mean wind speed over the interval of 1 hour prior to 6 hours after RL formation.Note the unstable T profiles at the ocean surface within the RLs.

Because the vertical salinity gradient and N_S^2 within RLs are constrained by surface inputs of freshwater and momentum, the magnitude of stabilization in RLs is primarily determined by rain rate and wind speed. Figure 2.9 displays the composite evolution of the salinity gradient from one hour prior to RL formation to six hours after RL formation. For a given wind speed (i.e., panels in a single row in Figure 2.9), the magnitude and depth of the upper ocean salinity gradient increases with increasing rain rate, reflecting a higher degree of stabilization within RLs forming under stronger rain rates. The impact of wind speed on RL formation is also evident in columns of fixed rain rate, as the magnitude of the upper ocean salinity gradient within RLs decreases with increasing wind speed. At wind speeds above 6 m s^{-1}, typically only the strongest rain rate cases are able to stratify the upper ocean for more than an hour, consistent with previous observations and theory (Thompson et al. (2019)).

It is noteworthy that RLs forming under weak rain rates (< 5 mm hr^{-1}) and weak surface winds (0-2 and 2-4 m s^{-1}), feature a persistent, stable vertical salinity gradient confined to the upper 1-2 m of the ocean (Figure 2.9). While the magnitude of stabilization is reduced in weak rain rate cases compared

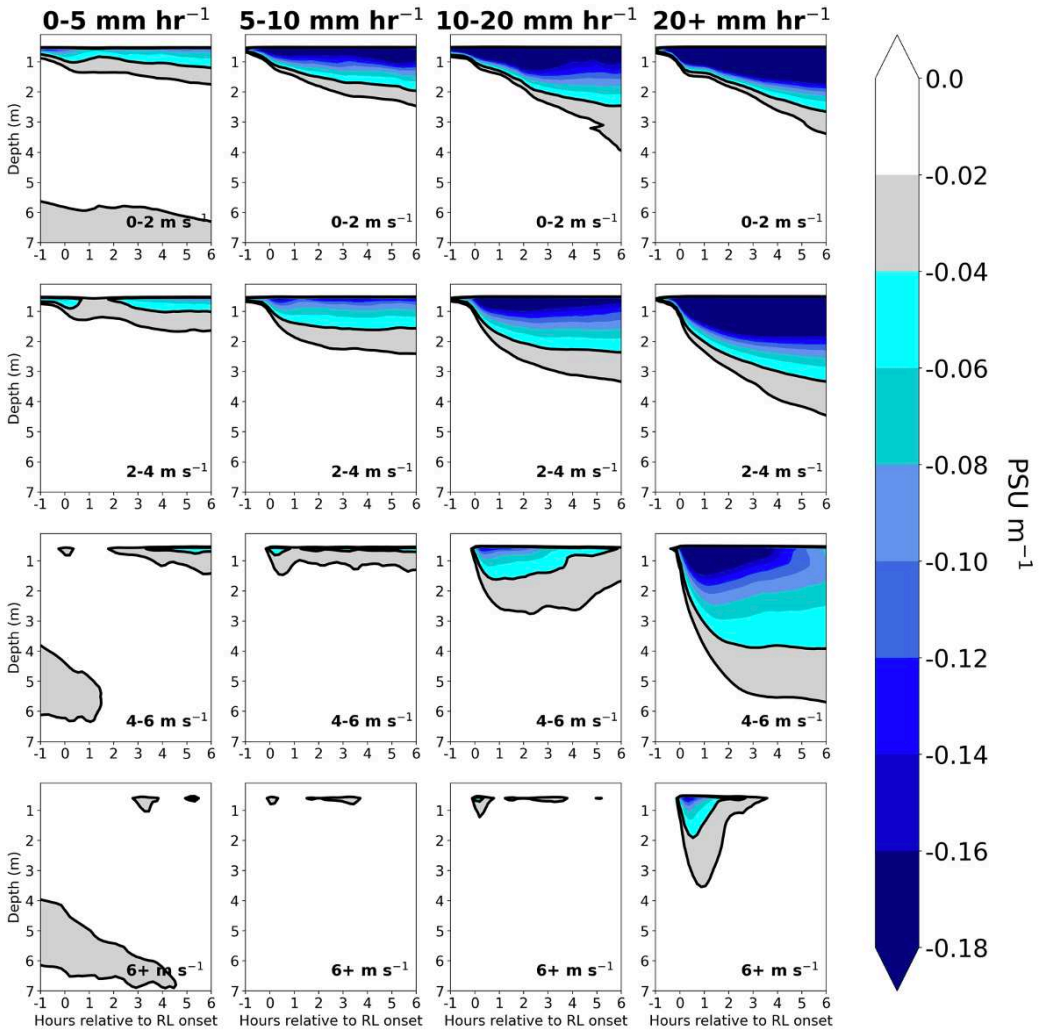

FIG. 2.9. Salinity gradient ($\frac{\partial S}{\partial z}$) within RLs binned column-wise by max rain rate from 60 minutes prior to 60 minutes after RL formation, and row-wise by mean wind speed over the interval of 1 hour prior to 1 hour after RL formation. Salinity gradient is computed as the centered difference (PSU m^{-1}) at 1-m intervals, and thus begins at a depth of 0.5 m.

to stronger rain rate cases, the stable salinity gradient in these cases is able to persist for many hours following RL formation. The implications of long-lasting RLs under low surface wind conditions are revisited in section 5.

When precipitation falls on a stably stratified upper ocean, vertical mixing of freshwater is further inhibited, resulting in RLs that feature a strong vertical salinity gradient and that are even more persistent than RLs that form over a well-mixed upper ocean. Figure 2.10 shows the composite difference in salinity gradient between RLs forming over a strongly stratified upper ocean with respect to N_T^2, defined as mean $N_T^2 > 1 \times 10^{-4}$ s^{-2} in the upper 5m of the column, compared to the salinity gradient for

all other RLs. Within the same rain rate and wind speed bins, RLs forming over an upper ocean that is strongly stratified with respect to N_T^2 feature a more intense salinity gradient in comparison to all other RLs (Figure 2.10). As there are few cases of RLs forming over strong upper ocean stratification at wind speeds above 6 ms^{-1}, wind speed bins in Figure 2.10 only extend to 6 ms^{-1}. This result conforms to the idealized model experiments of Iyer et al. (2021) that revealed larger salinity anomalies and delayed mixing in the upper ocean when rain falls on a stably stratified upper ocean compared to rain falling on a well-mixed upper ocean.

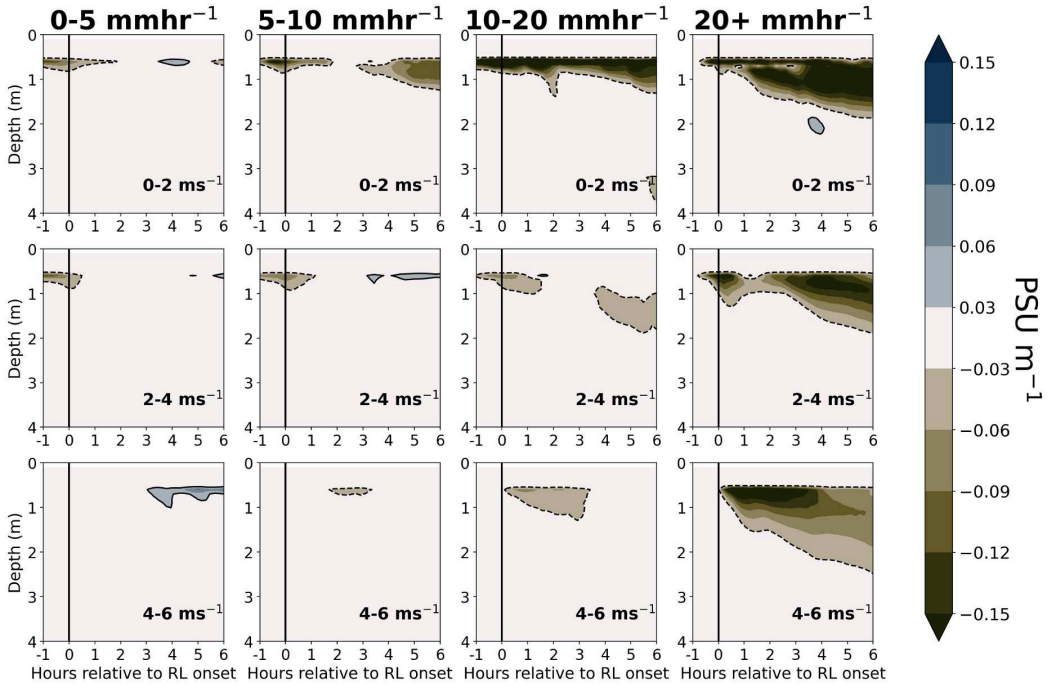

FIG. 2.10. Difference in salinity gradient between RLs forming over a strongly stratified upper ocean with respect to temperature (N_T^2 > 1e-4) and all RLs, from one hour prior to six hours after RL formation. Brown shading (negative) represents a stronger salinity gradient in RLs forming over a strongly stratified upper ocean, while blue shading (positive) represents a weaker salinity gradient in RLs forming over a strongly stratified upper ocean. Figure is binned column-wise by max rain rate from 60 minutes prior to 60 minutes after RL formation, and row-wise by mean wind speed over the interval of 1 hour prior to 1 hour after RL formation.

2.4.2 RL spatial dimensions

The footprint of contiguous cells with RLs ranges from as small as a single 2 km×2 km grid cell to as large as 97% of the 50 km×50 km domain. For purposes of estimating RL footprint size, the maximum number of adjacent grid points containing a RL for a given time step is computed, and a distribution of RL equivalent diameter is determined. Figure 2.11shows the frequency of RL equivalent diameter, with possible values of RL equivalent diameter spanning 2 km to 55.6 km. For time steps in which RLs are

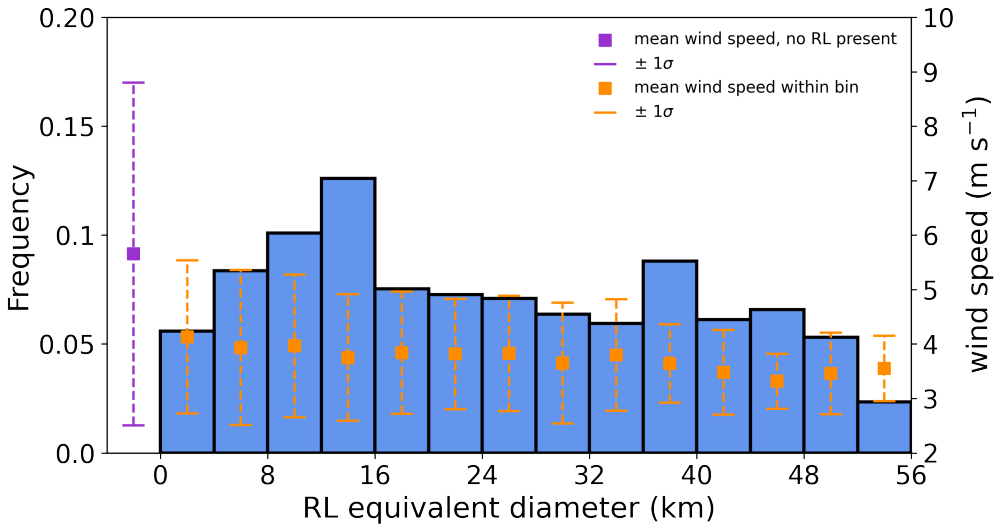

FIG. 2.11. Histogram of RL equivalent diameter frequency (blue), with domain-averaged wind speed $\pm 1\sigma$ overlaid for the corresponding bin (orange). RL equivalent diameter represents equivalent diameter of largest contiguous RL for time steps when RLs are present. The x-axis has been extended to include the domain-averaged wind speed $\pm 1\sigma$ for time steps when no RLs are present (purple).

present, the mean and median RL equivalent diameter of the largest RL present are 25 km and 23 km, respectively.

Evaluating domain-averaged wind speed within each RL equivalent diameter bin in Figure 2.11 shows consistent values of mean domain-averaged wind speed across all RL sizes. Within RL equivalent diameter bins, mean values of domain-averaged wind speed range from 3.32 m s^{-1} (RL equivalent diameter 44-48 km) to 4.13 m s^{-1} (RL equivalent diameter 0-4 km), compared to a mean domain-averaged wind speed of 5.65 m s^{-1} when no RLs are present. However, wind speed variability within each bin decreases with increasing equivalent diameter, indicating that the largest RL footprints are less likely to occur at higher wind speeds.

2.4.3 Reduced vertical mixing within RLs

In order to quantify the degree of mixing within RLs, the temperature tendency term in GOTM is decomposed into contributions from solar radiation and contributions from the sum of turbulent and viscous transport. The temperature tendency term in GOTM for a given level is defined as:

$$\dot{\theta} = \frac{\partial}{\partial z}\left((\nu_T^{\theta} + \nu^{\theta})\frac{\partial \theta}{\partial z}\right) + \frac{1}{C_p \rho_0}\frac{\partial I}{\partial z} \tag{2.6}$$

where $\dot{\theta}$ is the material derivative of potential temperature, ν_T^θ and ν^θ are the turbulent and molecular diffusivities of heat, respectively, C_p is the heat capacity of seawater, and ρ_0 is a reference density (Burchard et al. (1999)). Shortwave radiation, I is prescribed and treated as an inner heat source as a function of depth, z. The source due to shortwave radiation is computed by GOTM according to a double exponential law following Paulson & Simpson (1977), assuming Jerlov type I water. The sum of latent heat, sensible heat, and longwave radiation fluxes are computed by GOTM at each time step and is treated as a boundary condition for $\partial\theta/\partial z$. Thus, the first term on the right hand side of Eq. 2.6 represents temperature tendency from turbulent and viscous transport, and the second term represents a source term from shortwave radiation. We compute the profile of temperature tendency from transport as the difference between the total temperature tendency profile and the shortwave heating profile.

The vertical profile of temperature tendency due to transport over the course of RL lifetime as a function of wind speed at rainfall rate is shown in Figure 2.12. The negative tendency due to transport in the upper 1-2 m of the column immediately preceding and following RL formation is associated with decreased air temperature and surface input of cool freshwater surrounding RL onset. Transport cooling persists from +1 to +6 hours following RL formation but over limited depth compared to the short RL onset period, despite an unstable temperature stratification in the 0.5-1 m (Figure 2.8). We revisit the reduction in transport mixing following RL onset in the following section.

2.5 The potential for RL feedbacks to the atmosphere

Analyses shown in the previous section document the effects of RLs on ocean stability profiles. Here, we investigate the second science question posed in Section 1, namely, how RLs may affect the atmosphere. Ocean processes are communicated to the atmosphere through their effects on fluxes of heat, moisture, and momentum at the air-sea interface. Since our 1D ocean model configuration assumes zero lateral advection, ocean processes in our experiments only regulate fluxes of heat and moisture by modulating the SST.

2.5.1 RL regulation of SST and surface fluxes

Figure 2.13 displays the composite evolution of SST, air temperature at 2 m (T_{air}), specific humidity at 2 m (q_{air}), wind speed at 10 m, latent heat flux (Q_E), and sensible heat flux (Q_H) from six hours prior to six hours after RL formation. The sign convention for surface fluxes is that a negative flux or flux anomaly cools the ocean. First, we composite the aforementioned variables for RLs that form when the

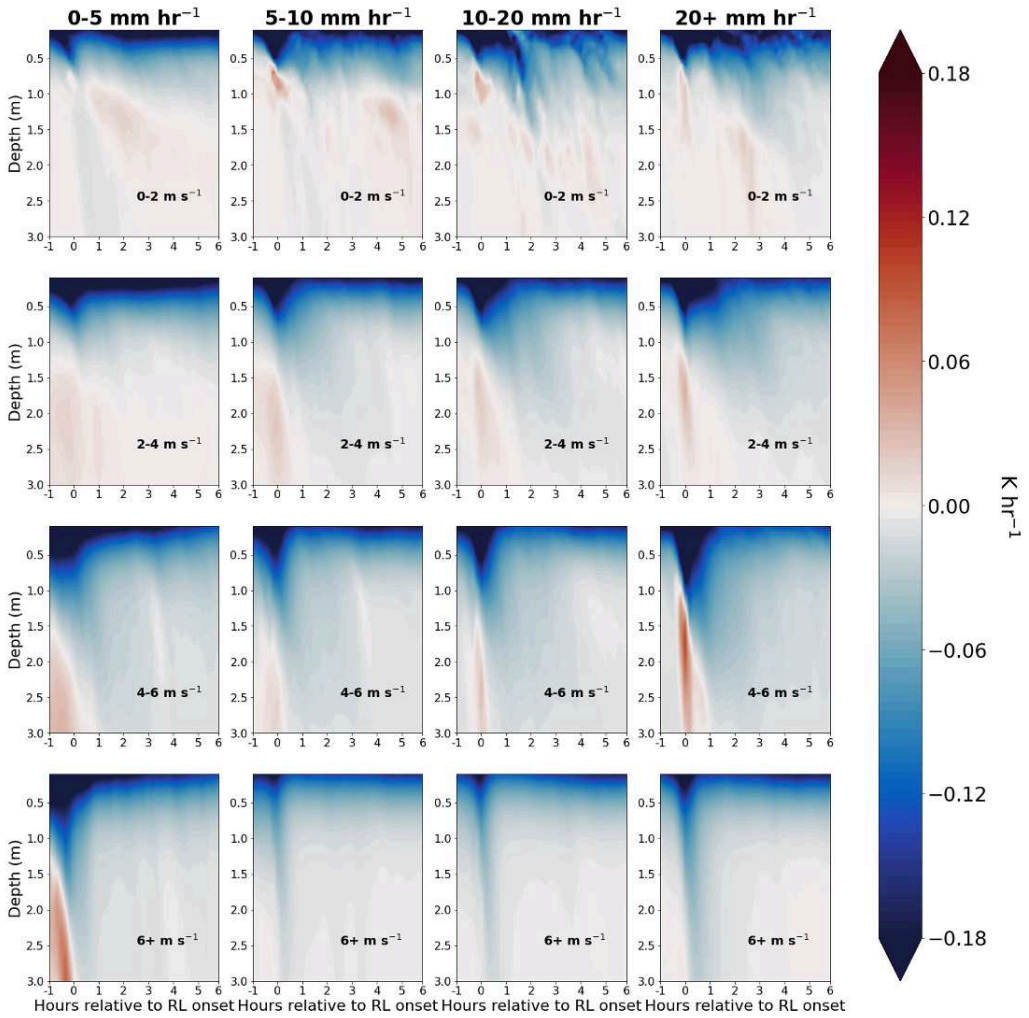

FIG. 2.12. Temperature tendency due to transport from one hour prior to six hours after RL formation. Figure is binned column-wise by max rain rate from 60 minutes prior to 60 minutes after RL formation, and row-wise by mean wind speed over the interval of 1 hour prior to 1 hour after RL formation.

wind speed averaged from -1 hour prior to +1 hour following RL formation is 4–6 m s^{-1} (left column of Figure 2.13). Second, we composite the variables for RLs that form when the maximum R from -1 hour prior to +1 hour following RL formation exceeds 20 mm hr^{-1} (right column of Figure 2.13).

While both SST and T_{air} decrease following RL genesis, the decrease in T_{air} is nearly an order of magnitude larger than the decrease in SST. Consequently, the sensible heat flux becomes more negative following RL formation, reflecting a greater flux of sensible heat into the atmosphere from the ocean. Similarly, negative departures in the latent heat flux occur immediately preceding and following RL formation, and generally persist for 3-4 hours following RL formation. Consequently, for all RLs, the enhancements (i.e., more negative departures) in Q_E and Q_H surrounding RL onset are attributed to

both the brief increase in wind speed at RL onset, as well as the more prolonged reductions in T_{air} and q_{air} following RL onset.

For RLs forming under a fixed background wind speed and different rain rates (left column of Figure 2.13), there is a systematic relationship between increasing rain rate, R, and larger negative departures of SST, T_{air}, q_{air}, Q_E, and Q_H in the ±1 hour span surrounding RL onset. However, for the higher R events ($R > 10-20$ mm hr^{-1}), Q_H is restored to pre-RL values more rapidly than in low R events, and Q_E departures become positive beyond 4 hours following RL onset. The heat flux response is the result of a decreased wind speed following RL formation in high R events, as well as a larger reduction in SST in high rain rate cases than low R cases. A similar response is seen in RLs forming under a fixed maximum R and different wind speeds (right column of Figure 2.13), with increasing wind speed generally associated with enhanced Q_E and Q_H in the ±1 hour span surrounding RL onset. The overall relationship between wind speed and fluxes within RLs (right column of Figure 2.13) is more difficult to assess than the relationship between R and fluxes within RLs (left column of Figure 2.13), as there is large variability within the wind speed bins in the hours following RL onset.

To quantify the role of rainfall in regulating stratification, surface fluxes, and SST perturbations, a second GOTM simulation was conducted over the same domain using identical ocean surface forcing as the first, except all precipitation fluxes were set to zero. Hereafter, we refer to the simulations with and without rain forcing as "RAIN" and "NO-RAIN", respectively. Thus, while rain does not fall onto the ocean in the NO-RAIN experiment, other forcing from the WRF output that is used in the RAIN experiment—T_{air}, wind speed, q_{air}, and net downwelling radiation—remains the same. Thus, any differences in stratification, surface fluxes, and SST between the two experiments arise purely from the presence of rainfall.

Figure 2.14 shows the difference in ΔSST, ΔQ_E, and ΔQ_H from Fig. 2.13 between the RAIN and NO-RAIN experiments for all RLs binned by R (left column) and wind speed (right column). Across all R and wind speed bins, SSTs reduction for several hours following RL formation is 0.05–0.1 K greater in the RAIN experiment, and hence within actual RLs, relative to the NO-RAIN experiment. Comparing the magnitude of SST reduction in RAIN (Figure 2.13) to that in NO-RAIN (Figure 2.14), the combined effects of cooling and stratification by rainfall can be seen to account for approximately 30–50% of the

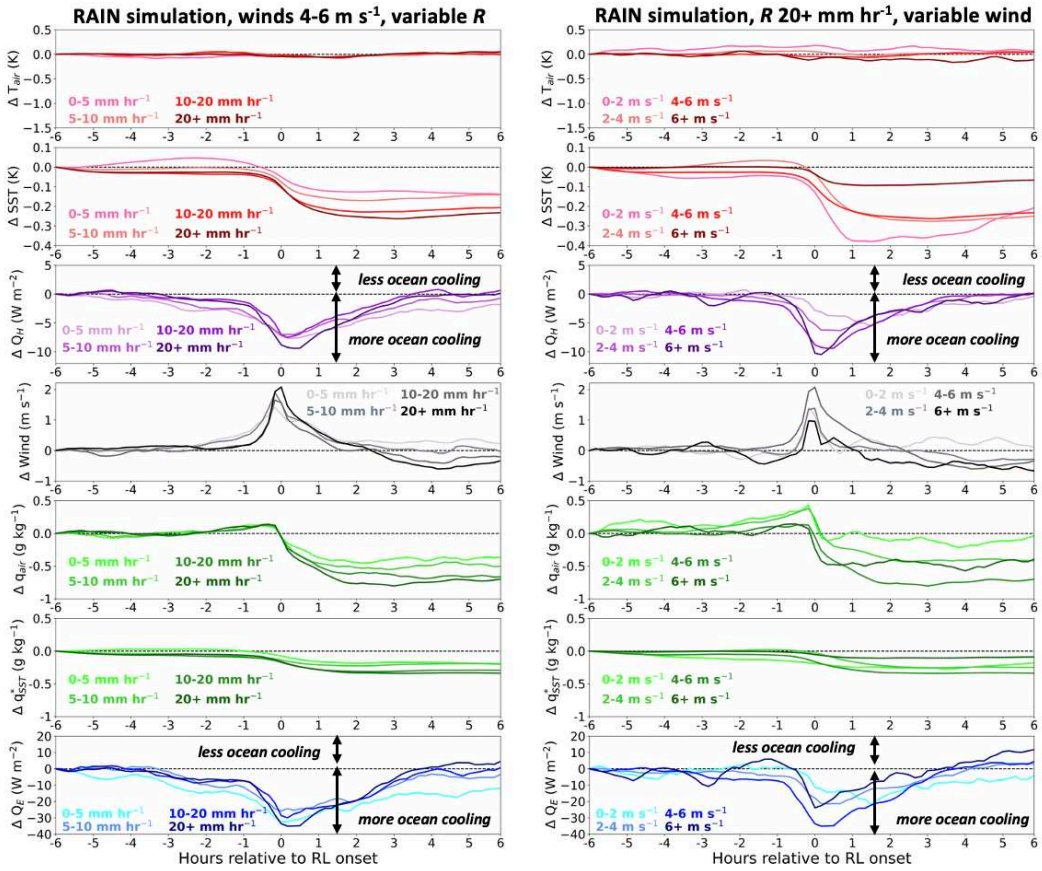

FIG. 2.13. Mean departure from 6 hours preceding RL onset (hour -6) of (top to bottom): air temperature at 2m (T_{air}); SST; sensible heat flux (Q_H); wind; specific humidity at 2m (q_{air}); saturation specific humidity at SST (q^*_{air}); and latent heat flux (Q_E). In the left column, the mean wind speed surrounding RL onset is fixed between 4-6 m s^{-1}, while rain rate varies; in the right column, the max rain rate preceding RL onset is fixed at > 20 mm hr^{-1}, while wind speed varies. Darkening color tone reflects increasing rain rate (left) and wind speed (right), for given bin. Fluxes are computed following Fairall et al., 1996, and a negative ΔQ_E or ΔQ_H indicates greater ocean surface cooling.

total SST reduction following RL onset. The influence of rain cooling on SST can be isolated to a rough approximated using wet-bulb temperature, SST, rain amount, and RL thickness:

$$\Delta T_{RL} \approx (T_{wetbulb} - SST) \cdot \frac{rain\ amount}{RL\ thickness} \tag{2.7}$$

Applying typical values of $T_{wetbulb} - SST$ = -5 K (Thompson et al. (2019)), rain amount = 10 mm, and RL thickness = 1 m to this equation, rain cooling alone can be estimated to reduce SST by 0.05 K.

The colder SST following RL onset in RAIN is reflected in the positive ΔQ_E and ΔQ_H differences in Figure 2.14, indicating weaker ocean-to-atmosphere surface fluxes compared to NO-RAIN. Unlike SST, however, ΔQ_E and ΔQ_H between the two simulations differ by less than 2% following RL onset.

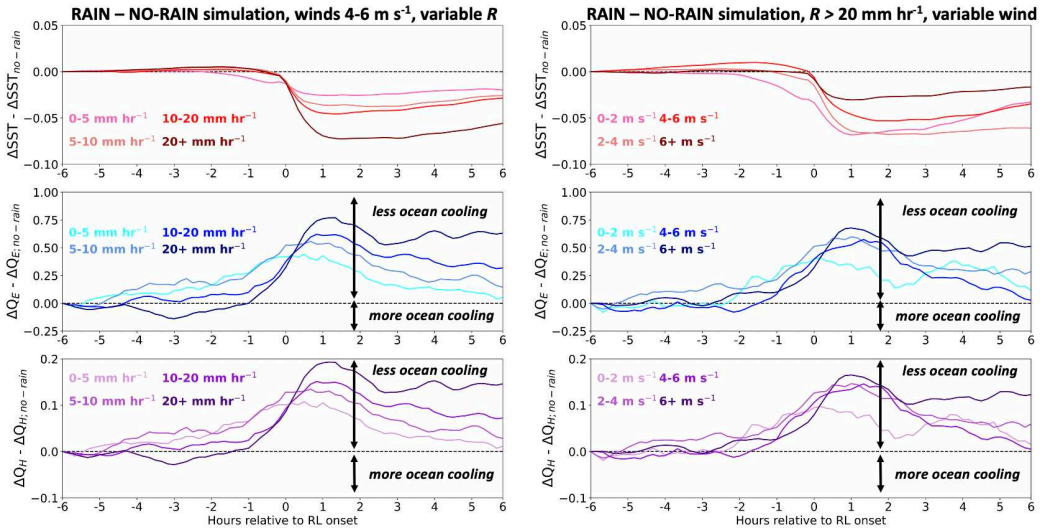

FIG. 2.14. Difference between simulation with and without precipitation forcing from -6 hours to +6 hours relative to RL onset of SST response from -6 hours (top, Kelvin), Q_E response from -6 hours (middle, W m^{-2}), and Q_H response from -6 hours (bottom, W m^{-2}). We note the change in vertical scale in all the plots. Note the persistent reduced SSTs following RL onset in the RAIN simulation in comparison to the NO-RAIN simulation.

This weak sensitivity of surface fluxes to RL-induced SST changes is a consequence of the much larger reductions of T_{air} and q_{air} than SST and q^*_{SST}, respectively, following RL onset (Figure 2.13). The composite time evolution of T_{air} surrounding RL onset follows a pattern typical of atmospheric cold pools (de Szoeke et al. (2017); Figure 2.13).

The reduced SST following RL onset in RAIN occurs despite the slightly weaker post-RL surface fluxes compared to those in NO-RAIN. We surmise that the colder post-RL SST in RAIN is the result of reduced downward transport of surface waters that have been cooled by the net heat transport out of the ocean. In essence, the salinity stratified RL in RAIN traps surface cooling within the RL, whereas cooled surface waters in NO-RAIN are readily mixed throughout the column.

The idea that RL salinity stratification concentrates surface cooling within the RL is supported by differences in total temperature tendency between the RAIN and NO-RAIN experiments, as shown in Figure 2.15. Because the temperature tendency from solar heating (the third term in Eq. 2.6) is identical in RAIN and NO-RAIN, any change in temperature tendency between the rain and no-rain simulations is the result of a change in the vertical transport term. For all wind speeds and R, cooling by vertical transport mixing is reduced following RL onset in RAIN when compared to NO-RAIN (i.e., red patches following RL onset). This occurs despite the near-surface unstable temperature stratification that exists within RLs (Figure 2.8).

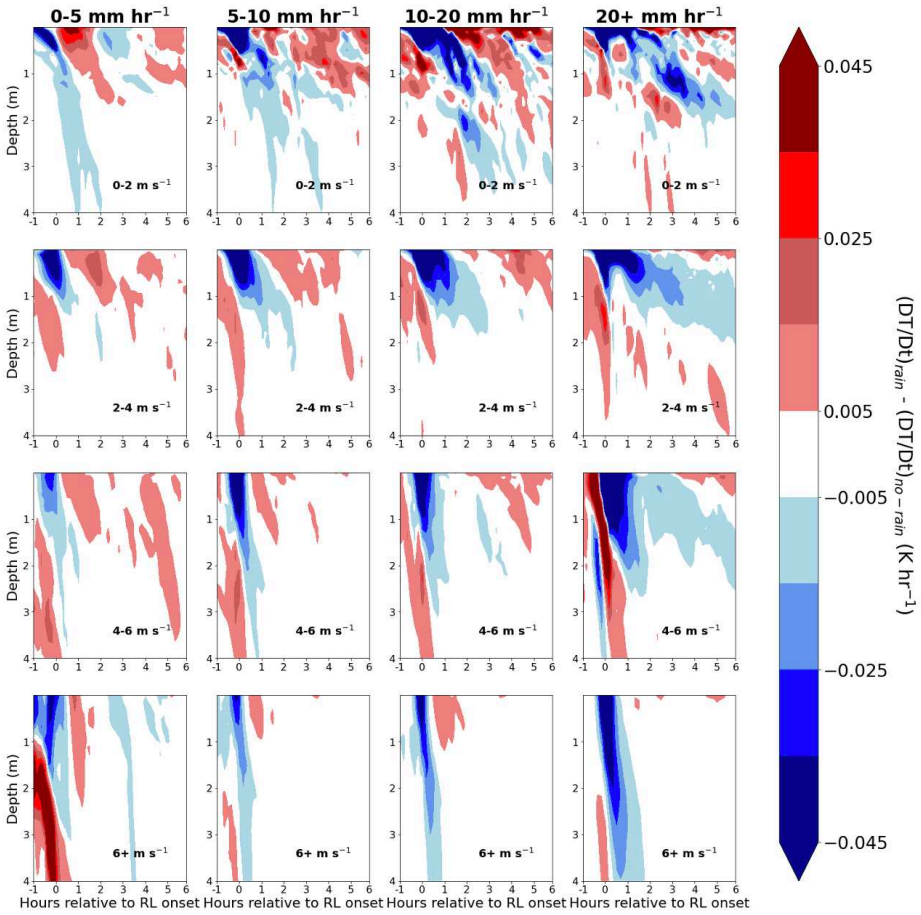

FIG. 2.15. Difference in temperature tendency between simulation with and without precipitation forcing from -1 hour to +6 hours relative to RL onset.

2.5.2 RL feedbacks via spatial SST gradients

While the difference in heat fluxes between RAIN and NO-RAIN is small, Figures 2.14 and 2.15 demonstrate that the role of precipitation on SST, and hence SST spatial gradients on the scale of RLs, may be large. Previous studies (Back and Bretherton (2009a); de Szoeke and Maloney (2020); Li and Carbone (2012); Lambaerts et al. (2020)) demonstrate that SST gradients force patterns of mass convergence and divergence within the marine boundary layer (MBL) that can initiate atmospheric convection. Here, we explore the role of precipitation in the creation of SST gradients.

Li & Carbone (2012) showed that for the West Pacific warm pool, assuming hydrostatic balance and given the Boussinesq approximation, the time derivative of surface wind convergence is proportional to the Laplacian of the SST field as given by the equation:

$$-(u_x + v_y)_t = w_{z,t} = \frac{p'_{xx} + p'_{yy}}{\bar{\rho}_b} = -\frac{gH}{\bar{T}_b}(T'_{xx} + T'_{yy}) \tag{2.8}$$

where $-(u_x + v_y)_t = w_{z,t}$ is the time derivative of surface wind convergence, p' is the pressure perturbation within a thin layer, ρ is air density, T' is the temperature perturbation within the MBL, H is the MBL height, and the subscript b denotes an environmental mean. SST anomalies influence MBL mass convergence and divergence through the right-most term in Eq. 2.8, which is the spatial second derivative, or the Laplacian, of T'. Because T' is partly set by SST (Back and Bretherton (2009a)), SST gradient contributions to low-level mass convergence are assessed with the SST Laplacian ($\nabla^2 SST$). In their analysis of four years of satellite observations of SST and rainfall, Li and Carbone found that approximately 75% of rainfall events over the West Pacific warm pool were spatially and temporally coincident with local surface convergence maxima, as estimated from the SST Laplacian. Furthermore, the onset of rainfall was more than twice as likely to be observed over $-\nabla^2 SST$ patches (corresponding to convergence) than over $+\nabla^2 SST$ patches (corresponding to divergence).

To explore the role of RLs in generating SST gradients, we compute the SST Laplacian for the GOTM RAIN and NO-RAIN simulations. For our analysis, $\nabla^2 SST$ is computed at every grid cell using adjacent cells in the model grid. Following Li and Carbone (2012), the SST Laplacian is reported in units of °C per 4 km^2 to convey the spatial scale of the gradients (Li and Carbone (2012)). Results are presented only for GOTM columns farther than two grid points from the domain boundary to avoid edge effects. Figure 2.16 displays the temporal evolution of domain-averaged zonal and meridional spectral density of SST Laplacian for RAIN and NO-RAIN. In the RAIN experiment, $\nabla^2 SST$ has a higher frequency of extreme values than $\nabla^2 SST$ in the NO-RAIN experiment, particularly during periods of increased precipitation and reduced winds (Figure 2.16). Using the median of the absolute values of $\nabla^2 SST$ as an estimate for the width parameter, we find a width parameter of 0.037 for the $\nabla^2 SST$ distribution in RAIN, which is nearly double the width parameter of 0.019 in NO-RAIN. This difference indicates that RLs, through their prolonged reduction of SST compared to adjacent RL-free columns, are capable of generating sharp SST gradients.

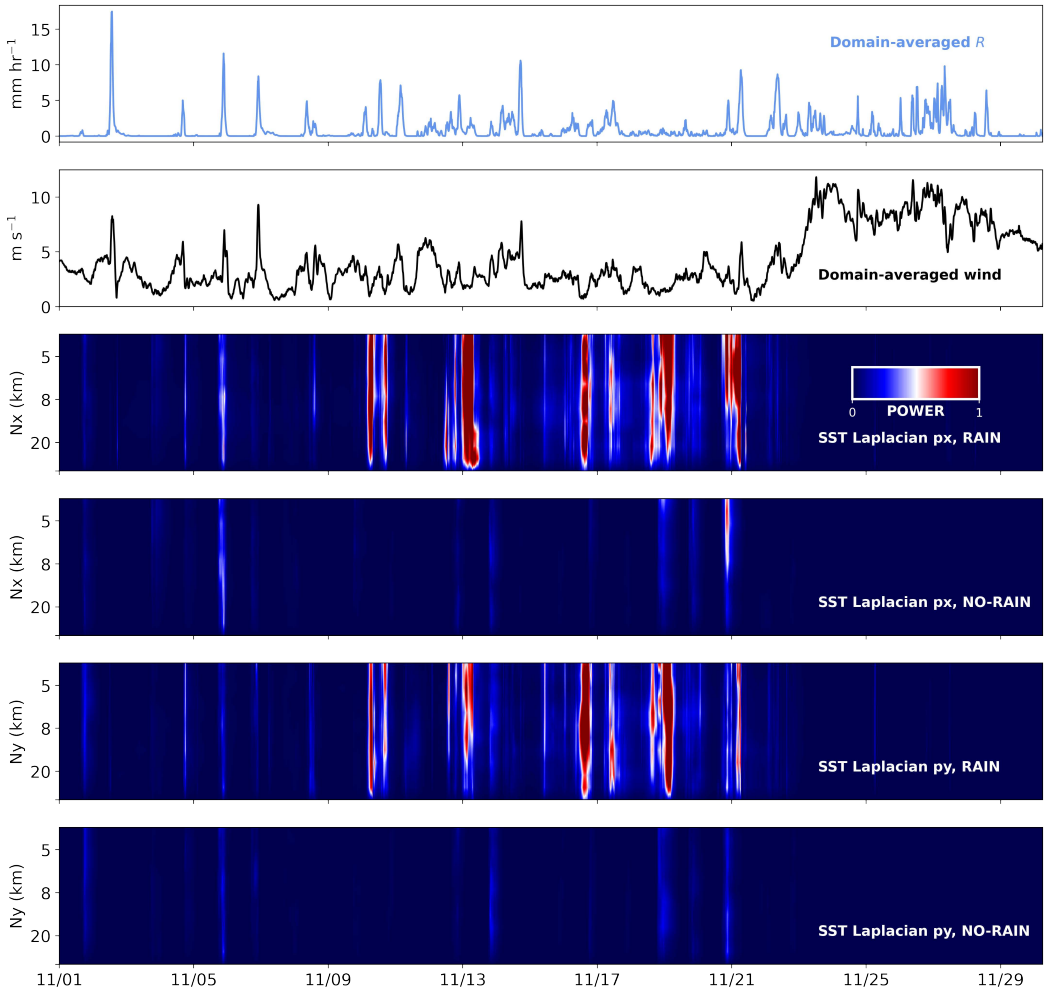

FIG. 2.16. Time series over the one-month simulation of (top to bottom): domain-averaged rain rate, domain-averaged wind speed, domain-averaged zonal spectral density of SST Laplacian for RAIN, domain-averaged zonal spectral density of SST Laplacian for NO-RAIN, domain-averaged meridional spectral density of SST Laplacian for RAIN, and domain-averaged meridional spectral density of SST Laplacian for NO-RAIN. Note: bottom four rows all use same color bar scale.

2.6 DISCUSSION

In this section, we synthesize results of the RAIN and NO-RAIN simulations, and offer some considerations for RL observation and the interpretation of our results. A conceptual aid in the form of a schematic illustration of atmospheric forcing and upper ocean response in RAIN and NO-RAIN, as well as the differences between the two simulations, can be seen in Figure 2.17.

For all RLs identified in RAIN, the reduced air temperature and humidity, as well as the increased wind speed and ocean-to-atmosphere surface turbulent fluxes following RL onset (Figure 2.13) are consistent with changes induced by convectively-generated cold pools (Feng et al. (2015); Yokoi et al.

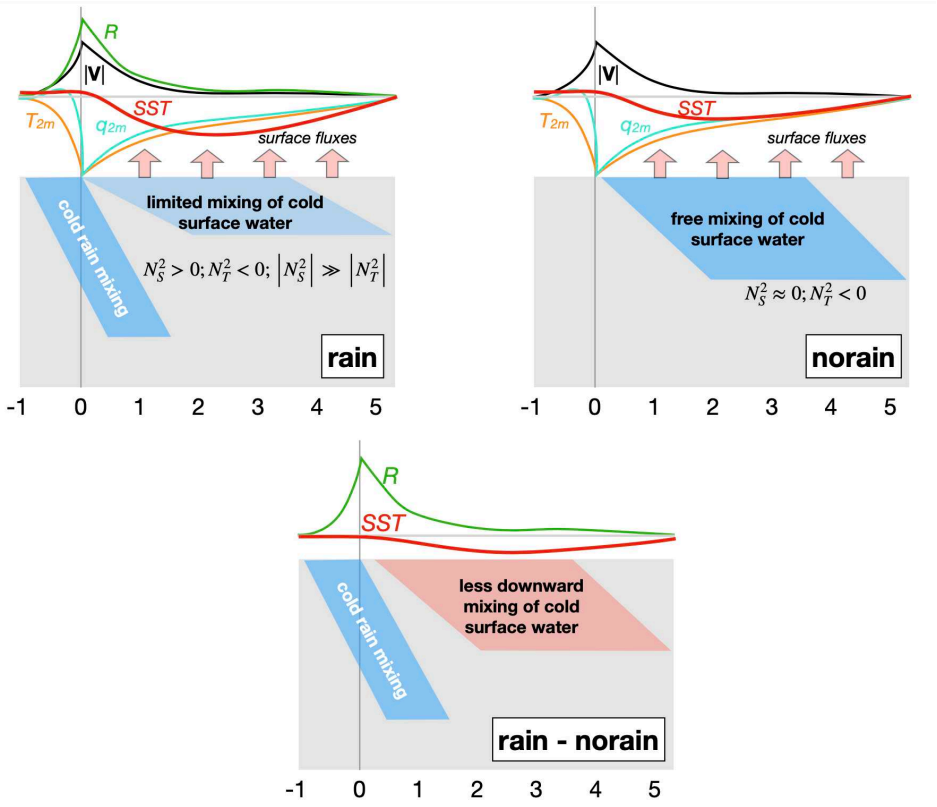

FIG. 2.17. Schematic illustration of atmospheric forcing and ocean response in RAIN (upper left), NO-RAIN (upper right), and the difference between the two simulations (bottom) for the upper few meters of the ocean and the period one hour prior and five hours following RL onset. Note in the RAIN - NO-RAIN panel, the only difference in atmospheric forcing is rainfall, which results in a cold rain input in the upper ocean around RL formation. After the initial cold rain input, the statically stable column in RAIN results in less vertical transport of heat and less subsurface ocean cooling than in NO-RAIN, confining the coldest water to the surface. Ocean-to-atmosphere surface flux differences between RAIN and NO-RAIN are less than 2% and are omitted from the bottom panel for clarity.

(2014); Zuidema et al. (2017)). The cold rain falling onto the ocean surface and the enhanced surface fluxes contribute to a sustained decrease in SST following RL onset. However, the cold SST signatures are evident even after surface flux perturbations have been restored to their pre-RL background states, suggesting a role for salinity stratification in regulating SST in RLs

The NO-RAIN simulation, which blocks rain from falling onto the ocean surface but otherwise forces the GOTM array with identical surface meteorology as in the RAIN simulaiton, confirms that salinity stratification by rainfall reduces the SST of RL-capped columns (Figure 2.14) by confining ocean water cooling to the near-surface layer (Figures 2.8 and 2.12). Furthermore, when rain falls onto a stably stratified upper ocean, such as onto a DWL, salinity stratification is amplified (Figure 2.10) and any

heat previously accumulated in the temperature-stratified layer is effectively "hidden" from the atmosphere (Wijesekera et al. (1999); Pei et al. (2018)) until the arrival of sufficiently strong winds capable of destroying the RL and mixing the cold surface waters with the warmer subsurface waters (Moum et al. (2014); Thompson et al. (2019)).

RLs reduce SST locally, creating a network of SST gradients and boundary layer convergence and divergence patterns that can initiate atmospheric convection. Our study demonstrates that RLs, through their intensification and prolongation of cold SST anomalies, sharpen regional SST gradients and increase the potential for SST gradient-driven surface convergence to influence atmospheric convection. Thus, RLs may affect the atmosphere in several ways: 1) they prolong locally reduced SST signatures, 2) they shield previously warmed ocean waters from the air-sea interface, thereby reducing ocean-to-atmosphere surface fluxes, and 3) they sharpen regional SST gradients beyond that which can be achieved solely by surface fluxes (Figure 2.16). It is important to note that the SST gradients and overall domain size in our simulations are much smaller than those in previous studies that connect SST gradients to initiation of atmospheric convection (Li and Carbone (2012); Skyllingstad et al. (2019)). We recommend further studies investigating RL feedback to the atmosphere using ocean-atmosphere coupled simulations over a larger domain.

Thompson et al. (2019) noted that even rain rates as low as $R = 5$ mm hr^{-1} are capable of forming RLs, and our results (Section 4.1) are consistent with this finding. At low wind speeds, weak R cases feature a persistent stable salinity stratification confined to the upper 1 m of the ocean (Figure 2.9), suggesting that even weakly forced RLs forming under these conditions can last for several hours. Observation of RLs under this forcing regime proves tricky, as stratification is confined to the upper 1-2 m of the ocean and requires high-resolution near surface measurements to capture changes to the water column. The persistence of a stable salinity stratification in weak R, low wind speed cases stresses the importance of towed profilers for ship-based observations that can sample the upper 2-3 m of the ocean outside the ship wake (Drushka et al. (2019b)) and, thus, capture changes to temperature and salinity under these conditions.

It is important to note that the 1-dimensional model framework implemented in this study presents a simplified view of ocean dynamics, neglecting the effects of horizontal processes. Lateral advection and propagation of salinity and temperature anomalies associated with RLs distributes SST and SSS anomalies over a greater area and smooths spatial gradients of these variables (Moulin et al. (2021)). As such, the extrema of SST gradients and the Laplacian of the SST field in section 4.4 are likely an

overestimate. The absence of lateral advection and the small model domain may also underestimate RL sizes (Figure 2.10). Larger RLs are hypothesized to occur using time-space conversion estimates from DYNAMO (Thompson et al. (2019)) and almost certainly occur based on the spatial extent of tropical mesoscale convective systems (Houze (2004)). We also note that some studies indicate that GOTM may overestimate SST reduction following precipitation (Pei et al. (2018)), although results from our model verification (Section 3) show that GOTM well reproduces observed SST under a variety of atmospheric conditions.

A challenge in using atmospheric model output as forcing data to compile RL statistics arises when assessing RL behavior many hours after formation. Idealized experiments allow for assessment of RL characteristics from single impulse rain rates (Drushka et al. (2016)) or an idealized evolution of rain and wind based on observations (Iyer and Drushka (2021b)). Forcing GOTM with WRF output provides complex and realistic atmospheric forcing conditions which aids understanding of RL duration, frequency, intensity, and size. Furthermore, the large number of RL-capped columns sampled over our month-long simulation allows for composite analysis of RL characteristics as a function of R and wind speed surrounding RL onset. However, as surface forcing conditions are constantly changing, it is difficult to account for further freshening events, changes to solar radiation input, high-frequency wind speed variability, and changes to 2 m specific humidity and temperature, all of which influence RL characteristics minutes to hours after RL formation. Because of these complications, we limit our composite analysis of RL intensity to six hours after RL formation.

Further studies are needed to understand the mesoscale characteristics of RLs globally and over extended periods of time. RL characteristics are determined by rain rate, wind speed, and background ocean stratification, and thus should have a unique presentation in different locations since these factors vary regionally and throughout time. Additionally, as background ocean stratification impacts RL intensity and duration, upper ocean state must be accounted for in RL climatology. Field campaigns that collect collocated, frequently sampled ocean-atmosphere observations, with fine vertical resolution in the upper ocean, are essential to improving our understanding of RL behavior and impact under different conditions.

2.7 Conclusions and summary

This study demonstrated that a 1D ocean model (GOTM) effectively replicates observed upper ocean temperature, salinity, and stability profiles in the equatorial Indian Ocean through a thorough

comparison with detailed observations of the combined ocean-atmosphere boundary layers from the DYNAMO field campaign. This result forms the basis for a detailed study on rain layer statistics from a 2D array of GOTM simulations forced by realistic atmospheric fields from the WRF atmospheric model.

The mean and median RL duration were found to be 4.5 and 1 hour, with a long tail to well over a day, mainly modulated by wind speed. RLs occur very infrequently for wind speeds over 8 m s^{-1}, consistent with the findings of Thompson et al. (2019). The rain layer equivalent diameter is quite uniformly distributed, with larger diameters related to slightly weaker winds on average. RLs reduce mixing due to their stable salinity stratification, which is modulated by the background stratification. RLs often feature unstable temperature stratification due to the low temperature of the initial rain impulse, and further surface cooling by enhanced surface fluxes driven by cold pool atmospheric temperature and humidity anomalies.

RL influence on the air-sea interactions was studied with a second 2D ocean simulation in which the rain from the atmospheric model was not allowed to fall on the ocean, so no RL formed, but all other atmospheric forcing fields were unchanged. Comparison between the RAIN and NO-RAIN simulations revealed that the presence of a RL leads to a reduction of SST that persists on time scales longer than the associated rain event. Approximately 1/3 of the SST reduction within RLs can be attributed to rain falling on the ocean surface, and thus, the RL itself, while 2/3 of the SST reduction can be attributed to other atmospheric fields (i.e. wind speed, q_{air}, T_{air}, and downward solar radiation). Analysis of SST response in RAIN and NO-RAIN highlights that RL influence on SST extends well beyond the lifetime of the source rain event. Salinity stratification in the RAIN simulation, and within RLs themselves, inhibits vertical transport of surface cooling to the deeper ocean, yielding SSTs approximately 0.1°C colder than in the NO-RAIN simulation.

To infer the feedback of the RLs to atmospheric convection, we studied the SST Laplacian, which is directly related to horizonal divergence in the atmosphere boundary layer. Evaluation of the distribution of SST Laplacian for RAIN and NO-RAIN revealed that the presence of RLs enhances the SST gradients considerably, with the median of the absolute value of the SST Laplacian increased by a factor 2. This result emphasizes the importance of coupled simulations investigating RL feedback to surface fluxes and atmospheric convection.

CHAPTER 3

A COLD LID ON A WARM OCEAN: INDIAN OCEAN SURFACE RAIN LAYERS AND THEIR FEEDBACKS TO ATMOSPHERE

3.1 INTRODUCTION

The Madden-Julian Oscillation (MJO) is an eastward propagating, planetary scale convective disturbance that circumnavigates the global tropics on time scales of 30–60 days (Madden and Julian (1971)). MJO influence on tropical climate ranges from intraseasonal time scales, where it is the dominant mode of tropical variability, to interannual time scales, where it influences the onset and evolution of El Niño Southern Oscillation (ENSO) events (McPhaden et al. (1988)). In addition to it's impact on tropical climate, diabatic heating anomalies from MJO convection perturb circulations in the extratropics and represent an important source of extratropical atmospheric predictability on subseasonal time scales (Hoskins and Karoly (1981); Weickmann (1983)).

Over the Indian and West Pacific Oceans, the MJO manifests as coupled regions of enhanced and suppressed cloudiness, referred to as the MJO active and suppressed phases, respectively. From the Eulerian perspective of the central Indian Ocean, an MJO event starts with the suppressed phase, characterized by large-scale subsidence, calm winds, shallow convection, light rainfall, and high outgoing longwave radiation (OLR) (Johnson et al. (1999)). As the disturbance propagates eastward, Indian Ocean suppressed conditions are gradually replaced with MJO active conditions, characterized by large-scale rising motion, increased winds, deep convection, heavy rainfall, and reduced OLR. Because of the slow propagation speed ($\sim$4-5 m s^{-1}) and large-scale nature of the MJO, the transition from convectively suppressed to convectively enhanced regimes occurs gradually over the course of several days. For this reason, it's helpful to define an intermediate MJO phase that describes the characteristics distinct to this transition period, referred to as the "transition" phase by the atmospheric science community and the "disturbed" phase by oceanography community (Pujiana et al. (2018); Thompson et al. (2019)). Hereafter, we refer to this intermediate phase as the "disturbed" phase, since the emphasis of this study is ocean influence on the MJO. MJO disturbed phase atmospheric conditions are characterized by cumulus congestus clouds and increasing rainfall relative to the suppressed phase, but without the strong westerly winds and deep convection evident during the active phase (Johnson et al. (1999); Moum et al. (2014); Thompson et al. (2019)).

In the tropical warm pool, the ocean mixed layer (analogous to the atmospheric boundary layer) temperature, salinity, and stability are strongly forced by surface meteorology (Halkides et al. (2015)). During the MJO suppressed phase, the combination of light winds and large surface solar heating warms the upper ocean and induces a stable temperature stratification, forming stable near-surface diurnal warm layers (DWLs; Bellenger & Duvel (2009); Soloviev et al. (1997); Woolnough et al. (2007)). Overnight, net surface heat flux out of the ocean cools and destabilizes the upper ocean, deepening the ocean mixed layer. (Bellenger and Duvel (2009); Thompson et al. (2019); Woolnough et al. (2007)).

Increased rainfall and cloudiness in the MJO disturbed phase deposits relatively colder, fresher, and less dense rain water on the ocean surface. Because wind speeds remain low to moderate during the disturbed phase, the less dense rain water frequently acts to stably stratify the upper ocean, forming near-surface rain layers (RLs; Asher et al. (2014); Drushka et al. (2016); Reverdin et al. (2012); Shackelford et al. (2022); Thompson et al. (2019); Wijesekera et al. (1999)). While DWLs and RLs can occur during all MJO phases, and can be present simultaneously, DWLs are most frequent during MJO suppressed phase and RLs are most frequent during MJO disturbed phase (Shackelford et al. (2022); Thompson et al. (2019)). The stabilizing buoyancy flux from surface heat and freshwater inputs during the active MJO is typically insufficient to withstand mixing by strong surface winds, and the ocean generally becomes well-mixed to the thermocline with a diurnally uniform SST during this period (Moum et al. (2014); Shackelford et al. (2022); Thompson et al. (2019)).

Ocean turbulent heat fluxes feed back to MJO convection through SST variability that is largely driven by MJO forcing and regulated by ocean stable layers. Anomalous high SST in DWLs during the suppressed phase enhances turbulent heat fluxes and reduces convective inhibition. This effect initiates convection and facilitates column moistening that "preconditions" the free troposphere to deep convection prior to the active MJO (Ruppert Jr. and Johnson (2016)). Additionally, increased SSTs ahead of MJO convection may support propagation and maintenance of MJO convection by enhancing surface fluxes and frictional moisture convergence (de Szoeke et al. (2015); DeMott et al. (2016); Zhang and Anderson (2003)). SST gradient-induced moisture convergence also plays an important role in recharging moist static energy (MSE) prior to the active MJO, and discharging MSE following the passage of MJO convection (de Szoeke and Maloney (2020)). Lower frequency modes of coupled ocean-atmosphere variability, including the Indian Ocean Dipole (IOD; Saji et al reference) and ENSO, have also been shown to influence the maintenance and propagation of MJO convection (DeMott et al.

(2015, 2018)). The importance of ocean feedbacks to MJO convection is evidenced by improved representation of the MJO in coupled versus uncoupled model simulations (e.g., DeMott et al. (2019); Kemball-Cook et al. (2002); Zhang et al. (2006)). In coupled simulations, high vertical resolution in the upper ocean and frequent ocean-atmosphere coupling further improve MJO representation, with the improvement in both cases attributed to better resolving the SST diurnal cycle (Bernie et al. (2005); Woolnough et al. (2007); Zhao and Nasuno (2020)).

While ocean feedback to the MJO via DWLs is well documented (Bellenger et al. (2010); de Szoeke et al. (2021); Ruppert Jr. and Johnson (2016); Woolnough et al. (2007)), the feedbacks associated with near-surface RLs to MJO convection are less explored. This can be partially explained by the large spatial scale and regular temporal nature of DWLs, which makes observation of these phenomena and their atmospheric feedbacks less complicated than those of RLs (Bellenger and Duvel (2009); Bellenger et al. (2010)). Regular observation of RLs has been further limited by the coarse vertical resolution and infrequent sampling of buoys and Argo floats. Thus, most observations of RLs have been collected with ship-based measurements (Asher et al. (2014); Drushka et al. (2019b); Iyer and Drushka (2021b); Thompson et al. (2019)) and drifters that profile the near-surface ocean (Reverdin et al. (2012)).

Because of observational constraints, idealized, single-column modeling experiments contextualized RL characteristics as a function of meteorological surface forcing and ocean background state (Drushka et al. (2016); Iyer and Drushka (2021b)). However, the idealized, 1D nature of these experiments provide limited information on RL behavior under realistic surface forcing and RL feedbacks to the atmosphere. Shackelford et al. (2022) studied RL formation under realistic atmospheric conditions by forcing a 2D array of 1D ocean column models using output from a convection-permitting simulation of the November 2011 DYNAMO event. Their findings highlight the role of RLs in reducing local SST through the surface input of cold rain, and maintaining and amplifying SST reductions through a stable salinity stratification that traps wind-driven evaporative cooling to the near-surface RL, corrobating results of previous model experiments (Pei et al. (2018)). Shackelford et al. also demonstrate the role of RLs in enhancing small-scale SST gradients that induce pressure perturbations in the atmospheric boundary layer and potentially excite atmospheric convection (Back and Bretherton (2009a); Li and Carbone (2012); Lindzen and Nigam (1987)). Pei et al. (2018) demonstrate that RLs may produce a slight subsurface ocean heating effect below the RL base, that is subsequently isolated from the atmosphere by the stable RL. Separating the subsurface ocean from the atmosphere could provide another

mechanism for RLs to influence the atmosphere. The incomplete understanding of RL feedbacks to the atmosphere motivates the following questions:

(1) What is the relative importance of RL generated SST gradients and RL-induced SST reduction in RL feedbacks to the atmosphere?

(2) How does the frequent separation of the subsurface ocean and the atmosphere during the MJO disturbed phase by RLs feedback to MJO convection?

This study utilizes a regional coupled ocean-atmosphere model to investigate the nature of RL feedbacks to the atmosphere. Section 2 provides details on the model and our simulations. Feedbacks to the atmosphere by SST gradients and reduced SST in RLs are analyzed in section 3, with an overall focus on how these effects vary as a function of MJO phase. We discuss the significance of these results in section 4 before presenting a concise summary and final conclusions in section 5.

3.2 METHODS

A description of the Scripps-KAUST Regionally Integrated Prediction System (SKRIPS) is provided in section 2.1. SKRIPS simulations used to evaluate RL feedbacks to the atmosphere are outlined in section 2.2.

3.2.1 SKRIPS model

The Scripps-KAUST Regionally Integrated Prediction System (SKRIPS) is a regional ocean atmosphere coupled model developed in a collaborative effort between Scripps Institute of Oceanography and the King Abdullah University of Science and Technology (Sun et al. (2019)). SKRIPS is comprised of an atmospheric solver, the Weather Research and Forecasting model (WRF; Skamarock et al., 2019), an ocean solver, the MITgcm (Marshall et al. (1997)), and a coupler, the Earth Systems Modeling Framework (ESMF) coupled driver (Hill et al. (2004)). The ESMF component is a two-way coupler that receives near-surface atmospheric variables (10-meter u- and v-wind components, 2-meter temperature and specific humidity, turbulent and radiative heat fluxes) and ocean surface conditions (SST and ocean surface velocity) that are then used to update the MITgcm surface forcing and WRF lower boundary conditions, respectively (Sun et al. (2019)). Surface turbulent heat fluxes are computed by WRF using the COARE bulk flux algorithm (Fairall et al. (1996, 2003)) and then passed to MITgcm by the coupler. SKRIPS output has been previously validated against atmosphere and ocean observations and reanalysis products in 30-day simulations of extreme heat events in the Red Sea region (Sun et al. (2019)), and in 14-day hindcasts of atmospheric river events over the Pacific Ocean (Sun et al. (2021)).

3.2.2 *Model experiments*

We investigate RL feedbacks to the atmosphere by running a 29-day SKRIPS simulation over the tropical Indian Ocean from November 1-30, 2011. This time period and location coincides with the November 2011 MJO event that was observed and studied during the Dynamics of the Madden-Julian Oscillation field campaign (DYNAMO; Yoneyama et al., 2013) The model is configured for a 10 ° by 10 ° domain centered on 75 E and 2.5 S (Figure 3.1), with 2 km horizontal grid spacing in both the ocean and atmosphere. Additionally, the 2 km horizontal grid spacing supports a convection-permitting WRF simulation. At convection-permitting scales (1-4 km), horizontal grid-spacing begins to approach the size of individual convective systems, "permitting" the removal of convective parameterizations from model simulations (Lucas-Picher et al. (2021)). The fine-scale horizontal grid spacing of these simulations provide a more realistic depiction of both atmospheric convection and upper ocean temperature and salinity response to rainfall, both of which are critical in evaluating RL influence on the atmosphere.

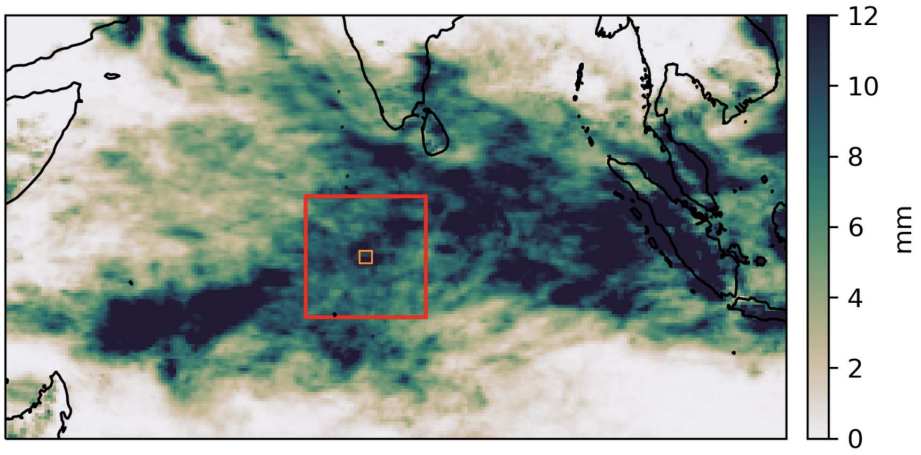

FIG. 3.1. CMORPH daily average rainfall (mm) for November 2011. The 10° by 10° model domain is outlined in red and the inner model domain used for computing ocean stability profiles in Figure 3 is outlined in orange.

Vertically, MITgcm is initialized on a stretched grid of 78 levels to a depth of 69.1 m, with 10 cm grid-spacing in the upper 2 m of the ocean and a telescoping vertical grid below 2 m. The MITgcm time step is 60 seconds and sub-grid scale horizontal mixing is parameterized using nonlinear Smagorinsky viscosities, while sub-grid scale vertical mixing is parameterized using the K-profile parameterization (Large et al. (1994); Sun et al. (2019)). WRF is initialized with 35 vertical sigma levels and a model top of 50 hPa. A summary of WRF parameterizations can be found in Table 1. Initial and boundary conditions

TABLE 3.1. WRF parameterizations

longwave radiation	Rapid Radiative Transfer Model for GCMs (Iacono et al. (2008))
shortwave radiation	Rapid Radiative Transfer Model for GCMs (Iacono et al. (2008))
microphysics scheme	Morrison 2-moment (Morrison et al. (2005))
PBL scheme	Mellor–Yamada–Nakanishi–Niino (Nakanishi and Niino (2009))
radiation time step	2 minutes
model time step	10 seconds

are provided by ERA-5 for the atmosphere (Hersbach et al. (2020)) and Hybrid Coordinate Ocean Model (HYCOM; Chassignet et al., 2007) reanalyses for the ocean, with lateral boundary forcing applied to both every 3 hours. WRF-MITgcm coupling frequency is set to 60 seconds, at which point WRF lower boundary forcing and MITgcm surface forcing are updated and applied.

To investigate the impact of RLs on the atmosphere, we conduct a second simulation over this domain with an identical model setup except that precipitation flux passed from WRF to MITgcm by the ESMF coupler is set to 0.0 at every time step. Therefore, in this second simulation, precipitation generated by WRF is prevented from falling on the ocean surface. We refer to the control experiment as *RL* and this second simulation as *no-RL*.

3.3 RL FEEDBACKS TO THE ATMOSPHERE

Here, we investigate two pathways in which RLs have the potential to influence the atmosphere. The first is the "SST gradient effect," wherein RL-induced SST gradients induce locally enhanced boundary layer convergence and convective initiation as well as locally enhanced divergence and convective suppression (section 3.1). The second, the more general "SST effect," describes both the direct effect of local SST reduction within RLs on atmospheric convection, and the delayed effect RL static stability may have on SST, and turbulent heat fluxes, by isolating the subsurface ocean from the atmosphere (section 3.2).

3.3.1 The SST gradient effect

The SST gradient effect refers to the hydrostatic adjustment of the marine boundary layer to SST gradients that force pressure-induced wind accelerations and drive patterns of low-level convergence and divergence (Back and Bretherton (2009a); Li and Carbone (2012); Lindzen and Nigam (1987)). While SST gradients that exist on large spatial scales ($\geq$100 km) and long time scales ($\geq$1 day) are accepted as a frequent precursor to atmospheric convection via the pressure perturbation mechanism, the transient nature and smaller-scale of rain-induced SST gradients have presented challenges in evaluating their impact on the atmosphere. In this section, we investigate the SST gradient pathway for RLs

to influence the organization and excitation of atmospheric convection within the confines of our coupled model simulations.

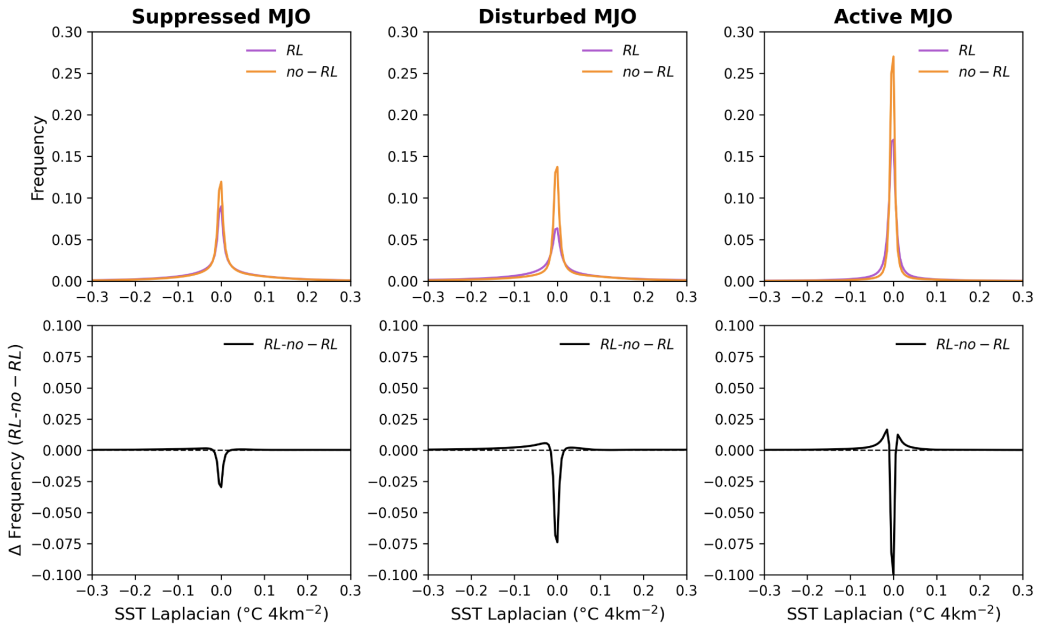

FIG. 3.2. Top: distribution of SST Laplacian for *RL* (purple) and *no-RL* (orange), composited column-wise by MJO phase. Bottom: change in SST Laplacian frequency (*RL* - *no-RL*), composited column-wise by MJO phase. Note that while differences between *RL* and *no-RL* distributions appear quite large in the MJO active phase, both distributions are narrowly peaked around 0 and large SST gradients in both simulations are uncommon during MJO active phase.

Li and Carbone (2012) showed theoretically that, for the West Pacific warm pool, the time derivative of surface wind divergence is proportional to the Laplacian of the SST field ($\nabla^2 SST$). Hence, we compute $\nabla^2 SST$ for both *RL* and *no-RL* at each grid cell to evaluate the role of RLs in generating and enhancing spatial SST gradients. $\nabla^2 SST$ is computed with adjacent grid cells using a 5-point stencil, and $\nabla^2 SST$ distribution for the two simulations can be seen composited by MJO phase in Figure 3.2. To quantify differences in the two distributions, we take the median of the absolute value of $\nabla^2 SST$ as an approximation of the width parameter of the underlying distribution, which reveals roughly a factor of 2 increase in the $\nabla^2 SST$ width parameter for *RL* (0.029) compared to *no-RL* (0.014) over the entire simulation. The factor of 2 increase in $\nabla^2 SST$ width parameter is consistent with findings of similarly constrained experiments conducted in a 1-dimensional ocean environment (Shackelford et al. (2022)). RL enhancement of SST gradients is most pronounced during the disturbed MJO, when $\nabla^2 SST$ width

parameter is nearly tripled in *RL* (0.048) compared to *no-RL* (0.017), while SST gradients in both simulations were greatly reduced during the active phase with *RL* and *no-RL* $\nabla^2 SST$ width parameters less than 0.001 (Figure 3.2).

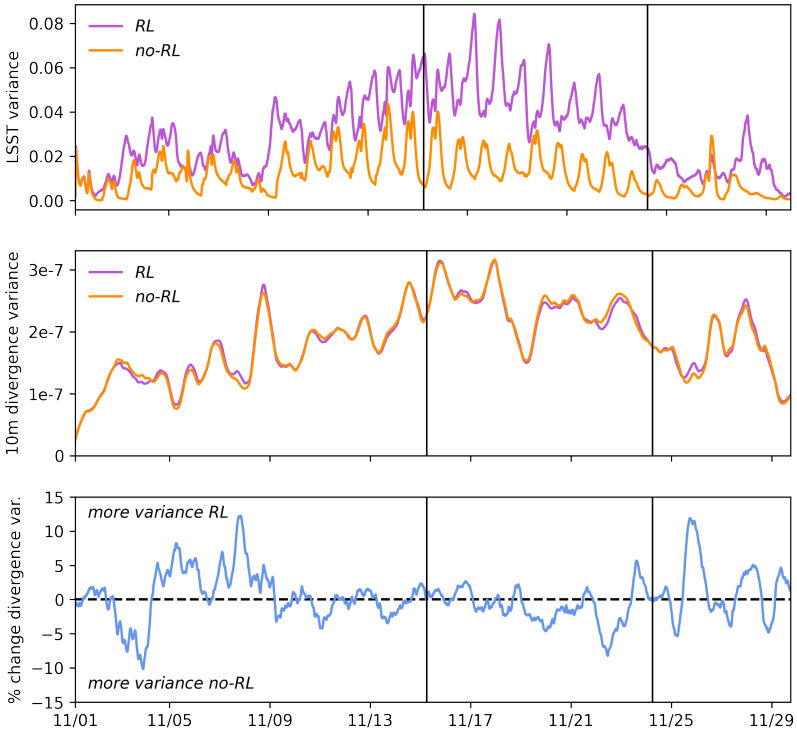

FIG. 3.3. Time series of domain mean values for (from top to bottom): SST Laplacian variance for *RL* and *no-RL*, 10 m divergence variance for *RL* and *no-RL*, and percent change in 10 m divergence (*RL-no-RL*). Divergence time series are presented as a 12-hour running mean. Vertical lines separate MJO phase.

RL feedback to the atmosphere through the SST gradient effect is evaluated by viewing the temporal coincidence between enhanced SST gradients and enhanced low-level convergence and divergence. Figure 3.3 displays time series of domain mean values for (from top to bottom): $\nabla^2 SST$ variance for *RL* and *no-RL*, 10 m divergence variance for *RL* and *no-RL*, and percent change in 10 m divergence (*RL - no-RL*). Time series of $\nabla^2 SST$ variance for *RL* and *no-RL* corroborate the findings of Figure 3.2 that RLs broaden the distribution of $\nabla^2 SST$ during the MJO suppressed and disturbed phases. The suppressed phase also features a 4 day period (11/05-11/09) in which 10 m divergence variance is roughly 5-10% larger in *RL* than *no-RL*. This period coincides with increased $\nabla^2 SST$ variance in *RL*, supporting the idea that RL-induced SST gradients may enhance low-level convergence/divergence. Figure 3.2 demonstrates that SST gradients are largest in *RL* during the disturbed phase, and differences in $\nabla^2 SST$

variance between *RL* and *no-RL* are also most evident during the disturbed phase (Figure 3.3). However, 10 m divergence variance is reduced in *RL* relative to *no-RL* during the disturbed phase, suggesting that RL-induced SST gradients may only influence the atmosphere during the suppressed phase, when large-scale forcing is weak. SST gradients in the active phase are small in both simulations, and therefore not expected to feed back to the atmosphere (Figure 3.2). The influence of RL-driven SST gradients on horizontal organization of convection was evaluated using the organizational index (I_{org}), but results from this analysis were inconclusive (not shown).

3.3.2 The SST effect

The SST effect refers to two distinct mechanisms in which RLs have the potential to influence the atmosphere by modifying SST. The direct SST effect results from RLs reducing SST locally through the input of cold rain to the relatively warmer ocean surface, and prolonging SST reductions through a stable salinity stratification that reduces downward mixing of evaporatively cooled near-surface water. The delayed SST effect, or delayed effect, arises from statically stable RLs isolating the subsurface ocean from the atmosphere. This separation of the subsurface ocean and atmosphere confines air-sea interaction to a near-surface cool layer, and limits exchange between the atmosphere and subsurface ocean heat in the presence of RLs.

3.3.2.1 Ocean and atmosphere state as a function of MJO phase

To evaluate the SST effect pathway, it is useful to begin by viewing upper ocean stability in the RL, or control, simulation as a function of MJO state. Figure 3.4 shows a time series of mean values of rain rate, wind speed, downwelling shortwave radiation, the temperature component of the buoyancy frequency (N_T^2), the salinity component of the buoyancy frequency (N_S^2), and the total buoyancy frequency (N_{T+S}^2) for the RL simulation over a 1° by 1° subdomain centered within the larger model domain (see Figure 3.1). Viewing these time series over a smaller subdomain presents a more coherent signal of ocean response to surface forcing, as signals from individual precipitation events would be lost over a larger area. Colorbars underlying the time series indicate MJO state. The three MJO phases exhibit distinct atmosphere and ocean characteristics, which are outlined below.

Suppressed MJO atmospheric state is characterized by infrequent rainfall, low winds, and high amounts of solar radiation impinging upon the ocean surface (Figure 3.4). The corresponding upper ocean stability profile is dominated by a diurnal cycle in N_T^2 and N_{T+S}^2, described by daytime stabilization through DWLs and nocturnal convection mixing upper ocean heat downward and deepening the OML. Sparse precipitation during the suppressed phase results in a generally well-mixed upper ocean

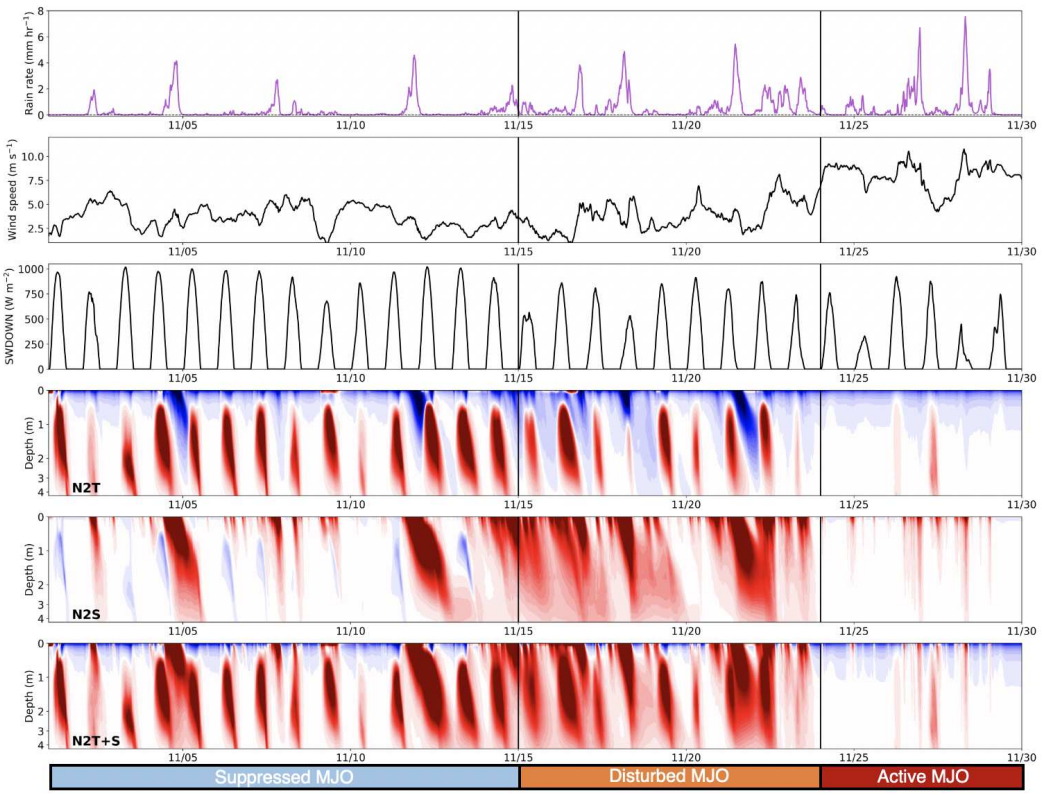

FIG. 3.4. Time series of mean values for *RL* simulation over 1° by 1° subdomain of: rain rate (mm hr^{-1}), wind speed (m s^{-1}), downwelling shortwave radiation at ocean surface (W m^{-2}), the temperature component of the buoyancy frequency for the upper ~4 m of the ocean (s^{-1}), the salinity component of the buoyancy frequency for the upper ~4 m of the ocean (s^{-1}), total buoyancy frequency for the upper ~4 m of the ocean (s^{-1}). 1° by 1° subdomain is centered within larger overall domain. Vertical lines separate MJO phase.

with respect to N_S^2, but low wind speeds enable the upper ocean to become readily stabilized during infrequent periods of enhanced rainfall (e.g., 11/04, 11/13).

As the MJO transitions from suppressed to disturbed conditions, atmospheric state features increasing rainfall, decreasing downwelling solar radiation, and gradually increasing wind speeds (Figure 3.4). This corresponds to an upper ocean that is frequently stably stratified near the surface with respect to N_S^2 and N_{T+S}^2, indicating a nearly constant presence of RLs during the disturbed phase. Note that for RLs in both suppressed and disturbed MJO conditions, salinity stabilization (N_S^2) far exceeds temperature destabilization (N_T^2), which allows the instability in the temperature stratification to persist within the overall statically stable column. While DWLs are present during the disturbed phase, their amplitude and frequency are reduced.

The MJO active phase is signified by a rapid increase in wind speeds followed by two large pulses of rainfall on November 26 and 28 (Figure 3.4). The convective envelope of the November 2011 MJO event

consisted of two convectively coupled Kelvin waves, resulting in the double pulses in wind speed and rain rate in Figure 3.4 during the MJO active phase (Moum et al. (2014, 2016)). While a brief relaxation in wind speed between the two pulses on November 27th allows for transient, weak stabilization in both N_T^2 and N_S^2, wind bursts at the leading edge of the two Kelvin waves induce turbulent mixing in the upper ocean that inhibits the formation of near-surface stable layers.

To quantify the effect of RLs on SST and their feedback to the atmosphere over the MJO lifecycle, we return to comparisons between *RL* and *no-RL*. Figure 3.5 displays time series of domain mean values for rain rate, wind speed, SSS, SST, and SST difference (SST_{RL}–SST_{no-RL}). While the differences in rainfall rate and wind speed between the 2 simulations are small, differences in SSS and SST are more evident. Since differences in SSS between the two simulations are expected and the explanation for these differences is apparent, we focus on differences in domain mean SST between *RL* and *no-RL*. The SST difference time series reveals two clear signals as a function of MJO state; first, a persistent reduced SST in *RL* relative to *no-RL* during the disturbed MJO (-0.029 K), and second, an increased SST in *RL* relative to *no-RL* during the active MJO (+0.022 K). Reduced SSTs in *RL* during the disturbed MJO can be explained by frequent RL presence leading to enhanced SST cooling through cold rain input on the ocean surface and concentration of evaporative cooling in the thin RL (Figure 3.5). However, the physical explanation for higher SSTs in *RL* during the active MJO, a period of intense precipitation, is not readily apparent in meteorological surface forcing as net surface heat flux is reduced in *RL* compared to *no-RL* during the MJO active phase. While SST differences between *RL* and *no-RL* during the MJO disturbed and active phases are small (∼0.03 K), this represents approximately 10-15 percent of the SST range throughout composite MJO events (0.2-0.3 K; DeMott et al., 2016), indicating that RL-induced SST changes modulate MJO SST range by 10-15%.

3.3.2.2 RL INFLUENCE ON THE TIMING AND INTENSITY OF MJO CONVECTION

The frequent presence of stable RLs during the MJO disturbed phase results in an extended period of time in which evaporative cooling is limited to a thin, cool, near-surface ocean layer yielding lower SSTs in *RL* during the disturbed MJO (Figure 3.5). Furthermore, the subsurface ocean becomes isolated from the atmosphere in the presence of RLs, thus reducing subsurface ocean mixing and altering vertical temperature profiles in the upper ocean.

Figure 3.6 displays a vertical profile of domain mean ocean temperature difference between *RL* and *no-RL*. RL signatures can first be identified as instances of lower near-surface ocean temperature in *RL* during the suppressed MJO. During the disturbed MJO, these signatures increase in area and frequency,

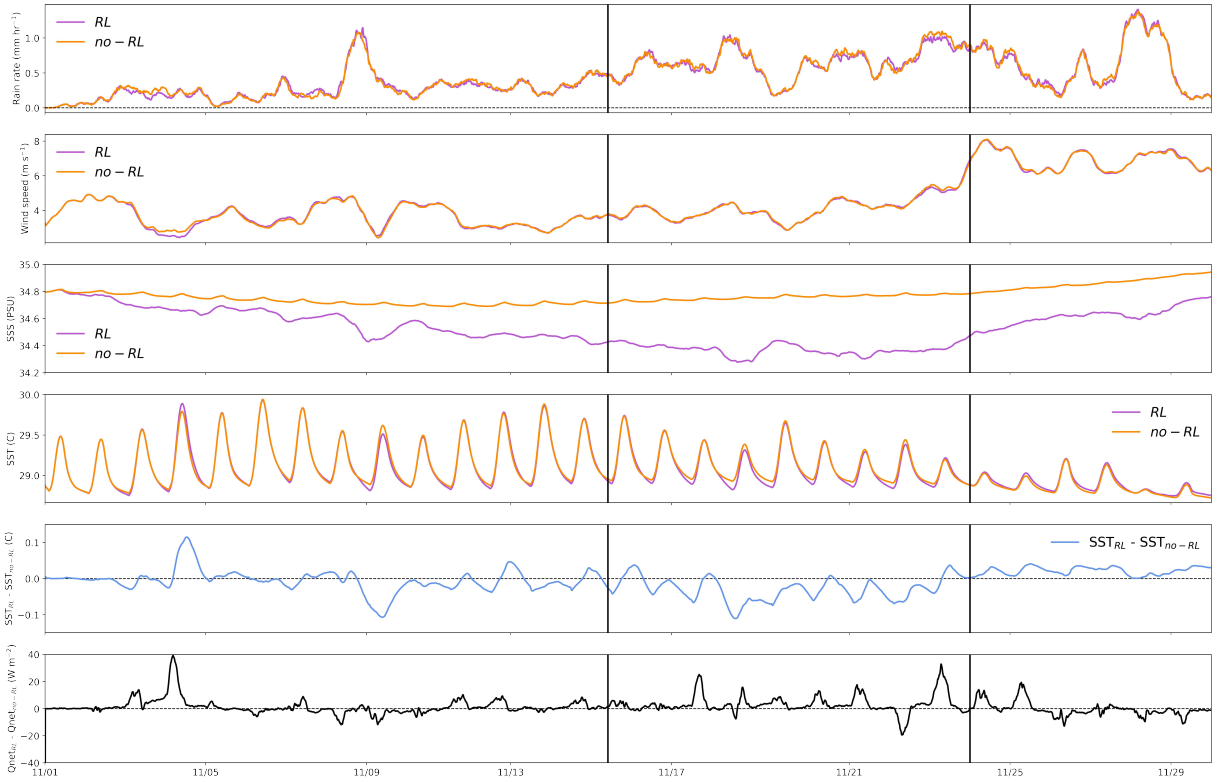

FIG. 3.5. Time series of domain mean values for *RL* (purple) and *no-RL* (orange) from top to bottom: rain rate (mm hr^{-1}), wind speed (m s^{-1}), sea surface salinity (PSU, g kg^{-1}), SST (C), SST difference (SST$_{RL}$-SST$_{no-RL}$), and net surface heat flux difference (Qnet$_{RL}$-Qnet$_{no-RL}$). Vertical lines separate MJO phase. To limit boundary effects, grid cells within 0.2° of each boundary are not included in domain mean.

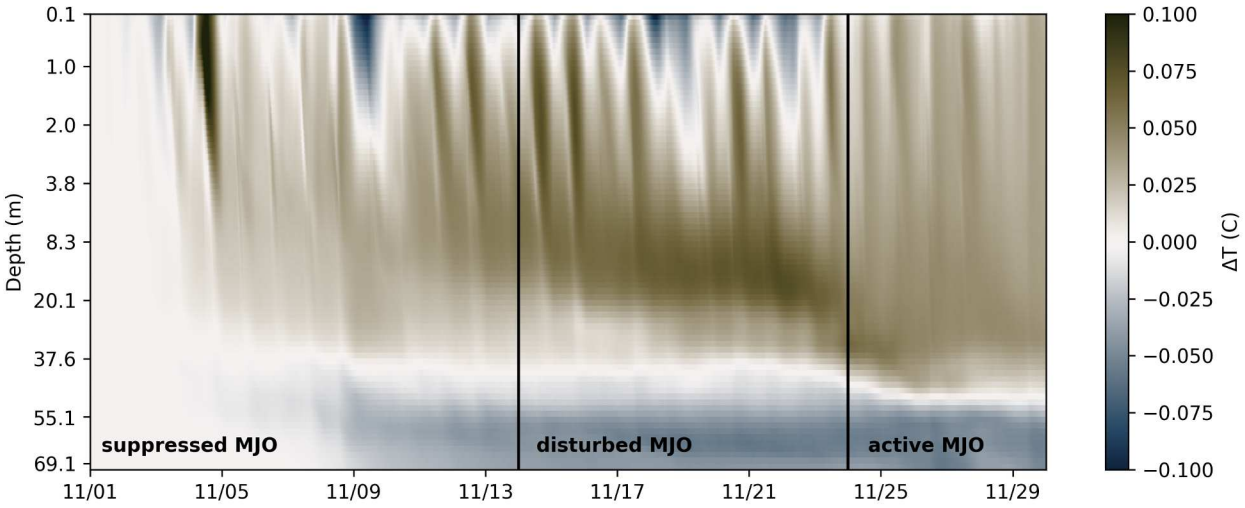

FIG. 3.6. Time series of domain mean vertical ocean temperature profile difference between *RL* and *no-RL* (T_{RL} - T_{no-RL}). Vertical lines separate MJO phase.

reflecting the increasing presence of RLs as the MJO from a suppressed to disturbed state. Beneath RLs, subsurface ocean mixing is reduced, resulting in relatively higher subsurface temperatures between 2-40 m in *RL* than in *no-RL*. With the arrival of the MJO active phase, RLs are eroded and subsurface ocean heat trapped by RLs during the disturbed phase is mixed to the ocean surface, raising SST. Thus, the build up of subsurface heat in *RL* relative to *no-RL* during the disturbed phase, and it's later release to the surface during the active phase represents a delayed pathway for the SST effect to feed back to MJO convection.

To this point, it remains unclear if RL-induced SST changes influence the structure and organization of convection. Qualitative comparisons of domain mean rain rate time series between *RL* and *no-RL* are inconclusive (Figure 3.5) and total accumulated rainfall in the two simulations is similar (∼1% less total rainfall in *RL*). To expand our investigation of RL feedbacks to convection over the MJO lifecycle, we evaluate select atmospheric variables as a function of both MJO phase and rain rate. Figure 3.7 shows, for the *RL* simulation and each MJO phase, from top row to bottom row: rain rate frequency, fractional contribution to total rainfall by rain rate, and mean OLR as a function of rain rate. Very light rain rates (R <0.01 mm hr^{-1}) dominate the rain rate frequency distribution during the MJO suppressed phase, but the distribution peak shifts towards slighty higher rain rates (0.01 mm hr^{-1} < R < 1 mm hr^{-1}) during the MJO disturbed and active phases. Fractional contribution to total rainfall by rain rate (Figure 3.6, middle row) varies little with MJO phase, although intermediate rain rates (1-10 mm hr^{-1}) make a relatively larger contribution to total rainfall during the MJO active phase, while heavy rain rates (>10 mm hr^{-1}) make a relatively smaller contribution. Mean OLR binned by rain rate decreases as rain rates increases for all MJO phases, with the lowest mean OLR values occurring during the MJO active phase.

We compute changes in rain rate frequency, fractional contribution to total rainfall by rain rate, and mean OLR by rain rate between *RL* and *no-RL* to asses the role of the SST effect in regulating convection across MJO phase. Figure 3.8 shows the same as Figure 3.7, but as percent change between *RL* and *no-RL*. For the same rain rate bins, cloud top temperatures in *RL* are warmer than those in *no-RL* during the suppressed and disturbed MJO, while cloud top temperatures are colder in *RL* during the active MJO. This suggests that for the same rain rate, clouds in *RL* are shallower than *no-RL* during MJO suppressed and disturbed phases, and deeper during MJO active phase. Figure 3.8 also shows that there is less rainfall in *RL* during the suppressed and disturbed MJO and more rainfall in *RL* during the active MJO. Furthermore, the underlying contribution of rain rate bins to total rainfall is shifted towards heavier

rain rates in *no-RL* during disturbed MJO state and heavier rain rates in *RL* during active MJO state (Figure 3.8).

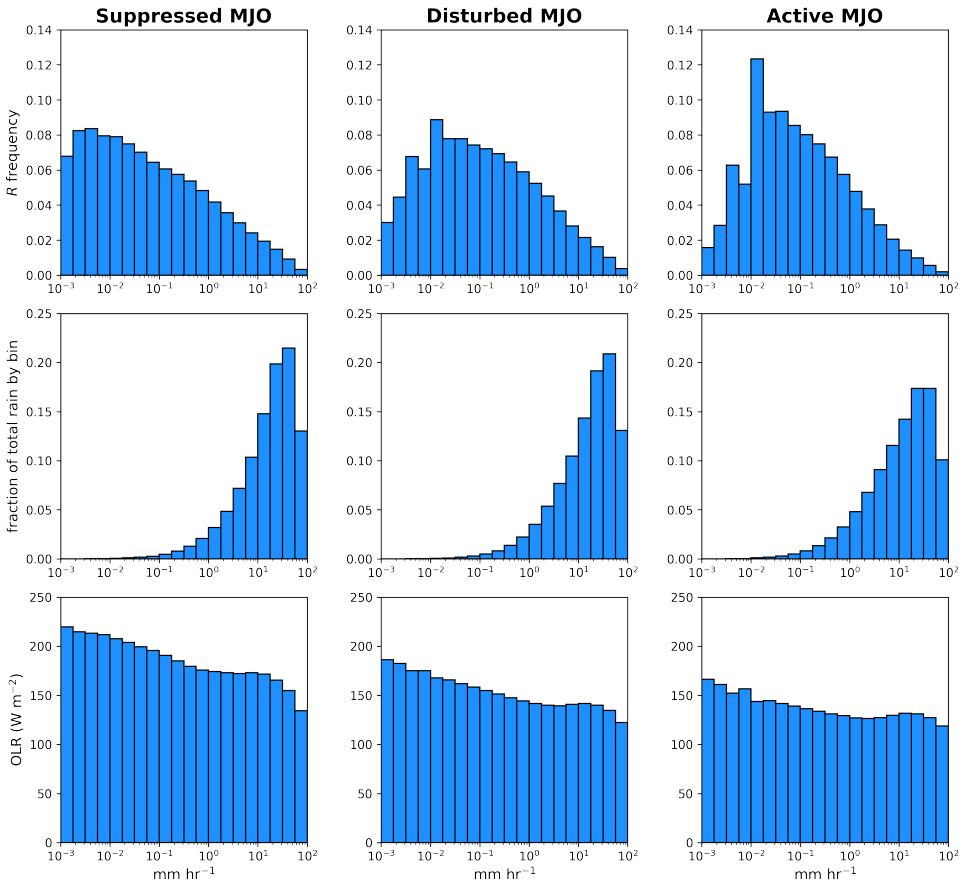

FIG. 3.7. From top row to bottom row: rain rate frequency, contribution to rainfall total by bin, and OLR, all binned by rain rate and composited column-wise by MJO phase.

While the rainfall rate perspective offered in Figure 3.8 suggests RLs do modify convection during the MJO lifecycle through the SST effect, it is also important to analyze changes to vertical structure of convection. RL influence on the vertical structure of convection via the SST effect may inhibit deep convection during the MJO disturbed phase when frequent RLs concentrate evaporative cooling in a thin near-surface layer, and support deep convection during the MJO active phase after westerly wind bursts erode RLs and release subsurface ocean heat to the surface (Figure 3.6). We evaluate RL influence on the vertical structure of convection by viewing percent change in vertical velocity variance (σ^2 w) between *RL* and *no-RL* as a function of MJO phase (Figure 3.9). During the MJO suppressed phase, σ^2 w is enhanced at low-levels but reduced at upper levels in *RL* relative to *no-RL*. We interpret the broader distribution of σ^2 w at low-levels in *RL* as the result of the SST gradient effect enhancing low-level

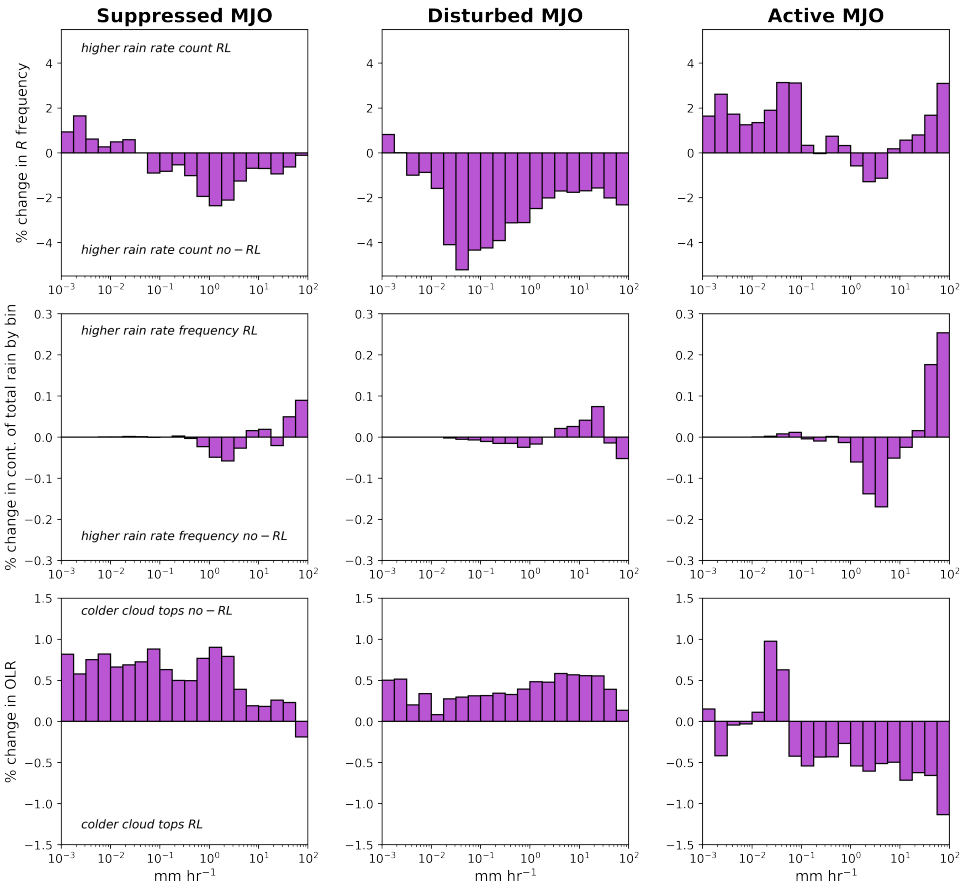

FIG. 3.8. Same as for Figure 6, but as percent change between *RL* and *no-RL*.

convergence under weak atmospheric forcing (Figure 3.3). When the MJO is in the disturbed phase, σ^2 w is reduced throughout the column in *RL* relative to *no-RL*, supporting the idea that RL-driven SST reduction inhibits deep convection and narrows the distribution of vertical velocity. In the active phase, the opposite effect is apparent, as σ^2 w is larger throughout the column in *RL*, as RL modification of ocean temperature and SST enhances deep convection during the MJO active phase and broadens the distribution of vertical velocity. This finding, coupled with Figure 3.8, demonstrates that RL-driven SST changes alter the intensity and vertical structure of convection during the MJO via the SST effect. In other words, RLs inhibit deep convection when the MJO is in it's disturbed state by reducing SSTs, while RLs support deep convection during the active MJO by maintaining a subsurface ocean heat reservoir during the disturbed MJO that is released to the surface upon the arrival of WWBs at the onset of the active MJO.

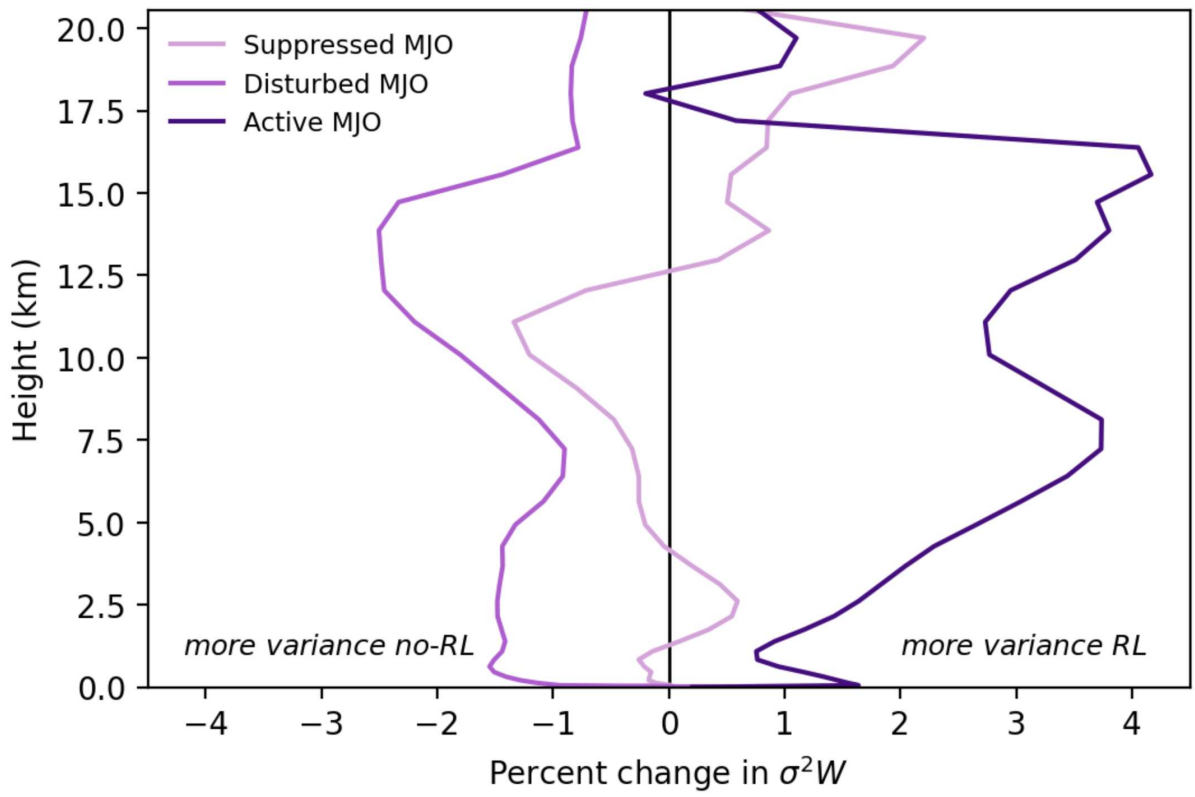

FIG. 3.9. Percent change in vertical velocity variance between *RL* and *no-RL*, composited by MJO phase.

3.4 DISCUSSION

Ocean surface rain layers (RLs) may feed back to the atmosphere through two distinct physical mechanisms, termed the SST gradient effect and SST effect.

Through the SST gradient effect, RLs feedback to the atmosphere by enhancing spatial SST gradients that alter patterns of surface wind convergence and divergence in the atmospheric boundary layer (Figure 3.2). Satellite observations and scaling analysis have shown that SST gradient-driven patterns of enhanced boundary layer convergence are associated with the onset of convection (Li and Carbone (2012)). We find that, compared to the $no-RL$ simulation, inclusion of RLs substantially broaden the distribution of SST gradients during the MJO suppressed and disturbed phases, but large-scale wind forcing in the MJO active phase results in a more uniform SST field with small SST gradients in both *RL* and *no-RL* (Figure 3.2). In the suppressed phase, when large-scale atmospheric forcing is weak, RL-induced SST gradients enhance low-level patterns of convergence and divergence, and slightly broaden the distribution of vertical velocity just above the atmospheric boundary layer (Figures 3.2 & 3.3).

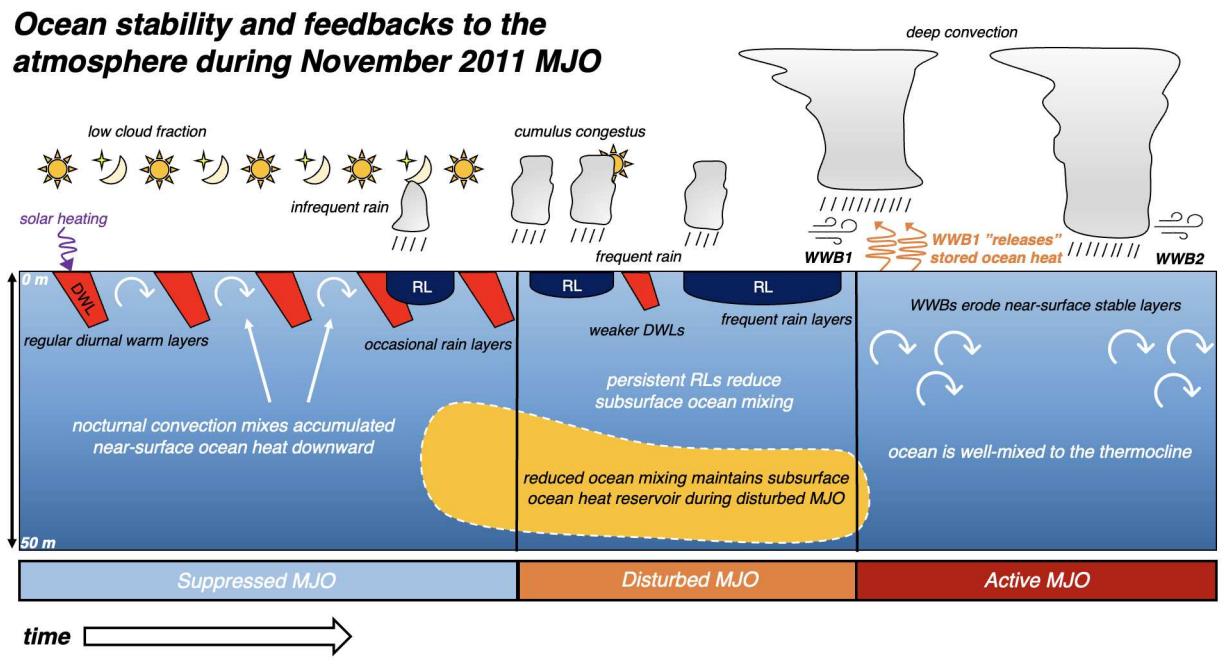

FIG. 3.10. Schematic illustration of the time evolution of ocean stability and RL feedbacks to the MJO during the November 2011 MJO event from a Eulerian viewpoint. MJO phase is denoted by the colorbar and time moves from left to right.

The SST effect describes distinct direct and delayed pathways in which RL-induced SST perturbations modify MJO convection (section 3.2). The direct SST effect results from RL-driven SST reductions while the delayed SST effect, or delayed SST effect, is a consequence of the separation of the subsurface ocean from the atmosphere by RLs during the disturbed MJO. Our findings demonstrate SST reductions in RLs during the MJO disturbed phase hinder atmospheric convection and narrows the distribution of vertical velocities throughout the troposphere (Figures 3.6, 3.8 & 3.9), demonstrating the effect of RL-induced SST changes on MJO convection. Additionally, we show that subsurface ocean heat that accumulates during the suppressed phase becomes isolated from the atmosphere during the disturbed phase when RLs constrain evaporative cooling to the near-surface ocean (Figure 3.6). At the onset of the MJO active phase, WWBs erode near-surface RLs and "release" the previously trapped subsurface ocean heat to the surface, raising SSTs in *RL* relative to *no-RL* (Figures 3.6). We find that the higher SSTs in *RL* during the active phase amplify the intensity of MJO convection and shift rain rate frequency from intermediate rain rates (1-10 mm hr^{-1}) to heavy rain rates (>20 mm hr^{-1}; Figures 3.7 & 3.8), thus presenting a delayed RL feedback mechanism. A schematic interpretation of the direct and delayed pathways of the SST effect is offered in Figure 3.10.

While results from our simulations reveal both the SST gradient effect and SST effect as viable RL feedbacks to the MJO, the SST effect is more pronounced. RL feedback via small-scale SST gradients is only evident during a brief period of the MJO suppressed phase, when RL-induced SST gradients enhance low-level convergence/divergence by ∼5-10% in *RL* compared to *no-RL* (Figure 3.3). During the disturbed phase, the SST gradient effect and SST effect have opposing feedbacks to convection, with RL-induced SST gradients potentially exciting convection, while RL-driven SST reduction inhibits convection. Despite large SST gradients in *RL* during the disturbed phase (Figure 3.2), convection is shallower and less frequent in *RL* than *no-RL* (Figure 3.8), indicating that RL feedback via the SST effect is more consequential during this period. Additionally, the largest changes in vertical velocity variance between *RL* and *no-RL* occur during the MJO active phase (Figure 3.9), when SST gradients are very small in both simulations. Instead, we attribute these changes to the "delayed" SST effect acting to reduce SST cooling in *RL*, thus enhancing MJO convection (Figure 3.5 & 3.6).

Reduced SST cooling during the MJO active phase in *RL* relative to *no-RL* is qualitatively consistent with similar experiments investigating the influence of salinity stratification on tropical cyclone intensity (TCs; Balaguru et al. (2020, 2022)). Balaguru et al. (2022) conduct coupled model simulations with and without rain coupling to the ocean surface (*RAIN* and *NO-RAIN*, respectively) and show that TC-induced SST cooling is reduced in the *RAIN* simulation. The reduction in TC-driven SST cooling is attributed to a stable salinity stratification that reduces vertical mixing and entrainment at the ocean mixed layer base (Balaguru et al. (2020, 2022)). Although wind-driven mixing in TCs may penetrate deeper than wind-driven mixing in the MJO active phase, the physical mechanism for reduced TC-driven SST cooling in Balaguru et al. (2022) is conceptually similar to reduced SST cooling in *RL* during the MJO active phase. However, this mechanism does not account for the build up of subsurface ocean heat during the MJO suppressed phase and maintenance of this subsurface ocean heat by RLs constraining air-sea interaction to the near-surface ocean, thus separating the subsurface ocean and atmosphere during the disturbed phase. We emphasize that the isolation of subsurface ocean heat during the MJO disturbed phase and reduced vertical mixing during the MJO active phase both play important roles in reducing SST cooling in *RL* during the active phase.

RL control on the intensity and periodicity of MJO convection through the "SST effect" suggests that accounting for RL-driven SST changes in MJO forecasting may improve MJO prediction (section 3.2). Due to the far-reaching influence of MJO diabatic heating anomalies on global weather and climate, more accurate representation of MJO convection aids not only short-term prediction of the MJO

itself, but also subseasonal forecasting in the extratropics. Our findings emphasize the importance of accounting for ocean RLs in coupled simulations. This requires coupled simulations with fine vertical grid-spacing in the upper ocean capable of explicitly resolving these features ($\leq$1 m), or, alternatively, the development of RL parameterizations that can communicate sub-grid impacts of RLs to coarser model dimensions. Improved MJO representation in coupled simulations with high resolution vertical grid-spacing in the upper ocean is typically attributed to better resolving the diurnal cycle in SST (Woolnough et al. (2007)). We speculate that in addition to resolving SST diurnal cycle and DWLs, resolving RL-induced SST changes may also be responsible for improved MJO simulation in these cases.

3.5 Conclusions and summary

In this study, we use SKRIPS, a regional coupled atmosphere-ocean model, to investigate feedbacks of ocean surface RLs to the atmosphere over the tropical Indian Ocean. We compared output from a control simulation (*RL*), which allows rain to fall onto the ocean surface, to that from an experiment (*no-RL*), which blocks rain from falling onto the ocean surface. These experiments aim to evaluate if RLs exert any detectable feedback to the atmosphere and MJO convection, and if that feedback is primarily driven by the SST gradient effect or the SST effect.

The SST gradient effect refers to the hydrostatic adjustment of marine boundary layer to small-scale SST gradients, which induces patterns of convergence and divergence and excites atmospheric convection. RLs generate and enhance spatial SST gradients by cooling the upper ocean through input of cold rain on the relatively warmer ocean surface, and maintaining and enhancing SST cooling by confining evaporative cooling to the thin RL. Comparing $\nabla^2 SST$ distributions for *RL* and *no-RL* demonstrates that RL presence is a significant contributor to the formation of small-scale SST gradients, consistent with the findings of Shackelford et al. (2022). The ability of RL-formed SST gradients in *RL* to enhance low-level convergence/divergence is most evident during a short period of the suppressed phase when forcing from the free troposphere is weak.

The "SST effect" feedback describes RL influence on MJO convection through distinct direct and delayed pathways. The direct "SST effect" arises from frequent RL presence during the MJO disturbed phase, which reduces SST and weakens deep convection. The delayed pathway is the consequence of RL stabilization of the upper ocean during the disturbed phase, which separates the subsurface ocean from the atmosphere and maintains a subsurface ocean heat source that is released to the surface following a westerly wind burst. The SST effect and SST gradient effect have opposing feedbacks to

convection during the disturbed phase, but inhibition of convection via the direct SST effect is more detectable than excitation of convection via the SST gradient effect. The delayed SST effect, which manifests as reduced SST cooling in *RL* relative to *no-RL* during the MJO active phase, amplifies deep MJO convection in *RL*, demonstrating an important influence of RLs throughout the MJO lifecycle.

CHAPTER 4

CONCLUSIONS AND FUTURE WORK

The work presented here aims to address questions surrounding 1) formation and characteristics of near-surface ocean rain layers (RLs), and 2) RL feedbacks to the atmosphere. Chapter 2 and 3 address these questions and a summary of those chapters is provided in 4.1 and 4.2, respectively. Section 4.3 highlights the the significance of these findings in the broader field of air-sea interaction, and offers strategies to leverage these findings in future work.

4.1 INDIAN OCEAN NEAR-SURFACE RL CHARACTERISTICS AND POTENTIAL ATMOSPHERIC FEEDBACKS

Recent studies have primarily investigated RL characteristics through idealized model simulations and observational analysis (Asher et al. (2014); Drushka et al. (2016); Iyer and Drushka (2021b); Thompson et al. (2019)). In chapter 2, we discuss results from 1-D ocean modeling simulations that build upon this previous body of work by incorporating spatially resolved and realistic atmospheric forcing. Fine-scale observations of the upper ocean collected during the Dynamics of the Madden-Julian Oscillation field campaign are used to verify the General Ocean Turbulence Model (GOTM; section 2.3). Spatiotemporal characteristics of equatorial Indian Ocean RLs are then investigated by forcing a 2D array of GOTM columns with realistic and well-resolved output from an existing regional atmospheric simulation (section 2.4). RL influence on the ocean-atmosphere system is evaluated through analysis of RL-induced modification to surface fluxes and sea surface temperature (SST). This analysis demonstrates that RLs cool the ocean surface on time scales longer than the associated precipitation event. A second simulation with identical atmospheric forcing to that in the first, but with rainfall set to zero, is performed to investigate the role of rain temperature and salinity stratification in maintaining cold SST anomalies within RLs. Approximately one third, or 0.1°C, of the SST reduction within RLs can be attributed to rain effects, while the remainder is attributed to changes in atmospheric temperature and humidity (section 2.5.1). The prolonged RL-induced SST anomalies enhance SST gradients that have been shown to favor the initiation of atmospheric convection (section 2.5.2).

4.2 RL FEEDBACKS TO THE MJO

In chapter 3, we explore the relative impacts of rain-induced SST gradients and rain-induced SST reduction on the atmospheric boundary layer using an ocean-atmosphere coupled model. Model simulations are run over the tropical Indian Ocean with fine grid-spacing both horizontally (2 km) and vertically in the upper ocean (10 cm), permitting the resolution of clouds and convective features in the

atmosphere, and also capturing rain-driven changes to near-surface ocean temperature and salinity. To examine the impact of rain-driven changes to the ocean surface on the formation and organization of atmospheric convection, we conduct a second model simulation where rainwater generated by the atmospheric model is prevented from falling onto the ocean surface. Comparisons between coupled simulations with and without rain-freshening of the ocean surface are used to investigate two RL feedback mechanisms, termed the SST gradient effect and SST effect. The SST gradient effect enhances surface convergence and divergence when large-scale forcing is weak during the MJO suppressed phase. The SST effect features both a direct and indirect feedback to the atmosphere. The direct SST effect arises from RL-induced SST reduction during the MJO disturbed phase, which inhibits atmospheric convection. The indirect, or delayed SST effect, is the result of RLs separating the subsurface ocean and atmosphere during the disturbed phase, which maintains an untapped reservoir of subsurface ocean heat. The subsurface ocean heat reservoir is brought to the surface with the onset of westerly wind bursts that mark the arrival of the MJO active phase, which acts to enhance MJO convection. Our results demonstrate that the SST effect has a larger impact on convection than the SST gradient effect, and that through the SST effect, RLs influence the intensity of MJO convection.

4.3 Future outlook

The results of this thesis indicate that near-surface RLs in the tropical warm pool feed back to the atmosphere and influence intraseasonal tropical variability through two mechanisms, the SST gradient effect and the SST effect. However, it remains unclear if the direct and delayed SST effect discussed in section 3.3 broadly applies to the MJO, or was a feature unique to the November 2011 MJO event. Future work could validate these findings by studying the direct and delayed SST effect across additional MJO events.

Results in chapter 3 emphasize the importance of accounting for RLs in MJO coupled simulations. This can be accomplished through coupled simulations with fine-scale vertical grid spacing in the upper ocean ($\leq$1 m), or through RL parameterizations that account for changes to the upper ocean occurring on finer vertical resolution than the model grid. As coupled simulations with very fine vertical grid spacing in the ocean are often computationally prohibitive, RL parameterizations may improve MJO simulation by regulating the intensity of convection throughout its lifecycle.

Numerous experiments have highlighted improvement in MJO prediction in coupled simulations compared to uncoupled simulations (e.g., DeMott et al. (2019); Kemball-Cook et al. (2012); Zhang et

al. (2016)). Additionally, MJO prediction in coupled model simulations further improves with more frequent air-sea coupling and higher vertical resolution in the upper ocean (Bernie et al. (2005); Woolnough et al. (2007); Zhao and Nasuno (2020)). While these further improvements in coupled simulations have previously been attributed to better representation of the SST diurnal cycle, we speculate in section 3.4 that this improvement could also be due to better representation of rain effects on temperature and salinity in the uppermost ocean model layers. Future work could investigate this by running coupled simulations similar to those discussed in section 3.2 (with and without rain coupling to the ocean surface) to assess if rain effects also contribute to improved MJO representation in coupled simulations with high vertical resolution in the upper ocean.

Previous studies investigating convective aggregation suggest SST plays an important role in regulating aggregation time scales (Coppin and Bony (2018); Holloway et al. (2017); Wing et al. (2017)). Additionally, it has been noted that ocean coupling may delay or inhibit convective aggregation (Coppin and Bony (2018); Holloway et al. (2017); Wing et al. (2017)), and some studies attribute this delay to SST gradients inducing low-level circulation patterns that oppose patterns favoring convective aggregation (Hogenegger and Stevens (2016)). Since our results investigating the influence of SST gradient effect and SST effect on the horizontal organization of convection are inconclusive, we recommend further studies investigating this relationship under realistic atmospheric conditions.

REFERENCES

Asher, W. E., A. Jessup, R. Branch, and D. Clark, 2014: Observations of rain-induced near-surface salinity anomalies. *Journal of Geophysical Research: Oceans*, **119**, 5483–5500, doi: 10.1002/2014JC009954.

Back, L. and C. Bretherton, 2009a: On the relationship between SST gradients, boundary layer winds, and convergence over the tropical oceans. *Journal of Climate*, **22 (15)**, 4182–4196, doi: 10.1175/2009JCLI2392.1.

Back, L. and C. Bretherton, 2009b: A simple model of climatological rainfall and vertical motion patterns over tropical oceans. *Journal of Climate, 22(23), 6477-6497*, **22 (15)**, 6477–6497, doi: 10.1175/2009JCLI2393.1.

Balaguru, K., G. R. Foltz, L. R. Leung, and S. M. Hagos, 2022: Impact of rainfall on tropical cyclone-induced sea surface cooling. *Geophysical Research Letters*, **49 (10)**, e2022GL098 187, doi: 10.1029/2022GL098187, e2022GL098187 2022GL098187.

Balaguru, K., G. R. Foltz, L. R. Leung, J. Kaplan, W. Xu, N. Reul, and B. Chapron, 2020: Pronounced impact of salinity on rapidly intensifying tropical cyclones. *Bulletin of the American Meteorological Society*, **101 (9)**, E1497 – E1511, doi: 10.1175/BAMS-D-19-0303.1.

Bellenger, H. and J. Duvel, 2009: An analysis of tropical ocean diurnal warm layers. *Journal of Climate, 22(13), 3629-3646*, **22 (13)**, 3629–3646, doi: 10.1175/2008JCLI2598.1.

Bellenger, H., Y. Takayabu, T. Ushiyama, and K. Yoneyama, 2010: Role of diurnal warm layers in the diurnal cycle of convection of the tropical Indian Ocean during MISMO. *Monthly Weather Review, 138(6), 2426-2433*, **138 (6)**, 2426–2433, doi: 10.1175/2010MWR3249.1.

Bernie, D. J., S. J. Woolnough, and J. M. Slingo, 2005: Modeling diurnal and intraseasonal variability of the ocean mixed layer. *Journal of Climate*, **18**, 1190–1202.

Broecker, W., 1991: The great ocean conveyer. *Oceanography*, **4**, 79–89, doi: 10.5670/oceanog.1991.07.

Burchard, H., B. K., and M. Villarreal, 1999: GOTM, a general ocean turbulence model: Theory, implementation and test cases. *Luxembourg Rep. EUR 18745*, pp.103.

Canuto, V., A. Howard, Y. Cheng, and M. Dubovikov, 2001: Ocean turbulence. part 1: One-point closure model-momentum and heat vertical diffusivities. *J. Phys. Oceanogr.*, **31 (6)**, 1413–1426, doi: 10.1175/1520-0485(2001)031<1413:OTPIOP>2.0.CO;2.

Chassignet, E. P., H. E. Burlburt, O. M. Smedstad, and G. R. Halliwell, 2007: The HYCOM (Hybrid Coordinate Ocean Model) data assimilative system. *Journal of Marine Systems*, **65 (1-4)**, 60–83, doi: 10.1016/j.jmarsys.2005.09.016.

Chen, S. S., R. A. Houze Jr., and B. E. Mapes, 1996: Multiscale variability of deep convection in realation to large-scale circulation in TOGA COARE. *Journal of the Atmopsheric Sciences*, **53 (10)**, 1380–1409, doi: 10.1175/1520-0469(1996)053<1380:MVODCI>2.0.CO;2.

Chen, S. S., et al., 2016: Aircraft observations of dry air, the ITCZ, convective cloud systems, and cold pools in MJO during DYNAMO. *Bulletin of the American Meteorological Society*, **97 (3)**, 405–423, doi: 10.1175/BAMS-D-13-00196.1.

Clark, N., L. Eber, R. Laurs, J. Renner, and J. Saur, 1974: Heat exchange between ocean and atmosphere in the eastern north pacific for 1961-1971. *Tech. Rep. NMFS SSR-682 NOAA, U.S. Dept. of Commerce, Washington, D.C.*

Coppin, D. and S. Bony, 2018: On the interplay between convective aggregation, surface temperature gradients, and climate sensitivity. *Journal of Advances in Modeling Earth Systems*, **10 (12)**, 3123–3138.

Costa, A. A., W. R. Cotton, R. L. Walko, and R. A. Pielke Sr., 2001: Coupled ocean-cloud-resolving simulations of the air–sea interaction over the equatorial western Pacific. *Journal of the Atmospheric Sciences*, **58 (22)**, 3357–3375, doi: 10.1175/1520-0469(2001)058<3357:COCRSO>2.0.CO;2.

Cronin, M. and M. McPhadden, 2002: Barrier layer formation during westerly wind bursts. *Journal of Geophysical Research*, **107**, doi: 10.1029/2001JC001171.

de Szoeke, S. P., J. B. Edson, J. R. Marion, C. W. Fairall, and L. Bariteau, 2015: The MJO and air–sea interaction in TOGA COARE and DYNAMO. *Journal of Climate*, **28 (2)**, 597 – 622, doi: 10.1175/JCLI-D-14-00477.1.

de Szoeke, S. P. and E. Maloney, 2020: Atmospheric mixed layer convergence from observed MJO sea surface temperature anomalies. *Journal of Climate*, **33 (2)**, 547–558, doi: 10.1175/JCLI-D-19-0351.1.

de Szoeke, S. P., T. Marke, and W. A. Brewer, 2021: Diurnal ocean surface warming drives convective turbulence and clouds in the atmosphere. *Geophysical Research Letters*, **48 (4)**, doi: 10.1029/2020GL091299.

de Szoeke, S. P., E. D. Skyllingstad, Z. Paquita, and A. S. Chandra, 2017: Cold pools and their influence on the tropical marine boundary layer. *Journal of the Atmopsheric Sciences*, **74 (4)**, 1149–1168.

DeMott, C. A., J. Benedict, N. P. Klingaman, S. J. Woolnough, and D. A. Randall, 2016: Diagnosing ocean feedbacks to the MJO: SST-modulated surface fluxes and the moist static energy budget. *Journal of Geophysical Research: Atmospheres*, **121**, 8350–8373, doi: 10.1002/2016JD025098.

DeMott, C. A., N. P. Klingaman, W.-L. Tseng, M. A. Burt, Y. Gao, and D. A. Randall, 2019: The convection connection: How ocean feedbacks affect tropical mean moisture and MJO propagation. *Journal of Geophysical Research: Atmospheres*, **124 (22)**, 11 910–11 931, doi: 10.1029/2019JD031015.

DeMott, C. A., N. P. Klingaman, and S. J. Woolnough, 2015: Atmosphere-ocean coupled processes in the Madden-Julian Oscillation. *Reviews of Geophysics*, **53**, 1099–1154, doi: 10.1002/2014RG000478.

DeMott, C. A. and S. A. Rutledge, 1998: The vertical structure of TOGA COARE convection. part i: Radar echo distributions. *Journal of the Atmospheric Sciences*, **55 (17)**, 2730–2747, doi: 10.1175/1520-0469(1998)055<2730:TVSOTC>2.0.CO;2.

DeMott, C. A., B. O. Wolding, E. D. Maloney, and D. A. Randall, 2018: Atmospheric mechanisms for MJO decay over the maritime continent. *Journal of Geophysical Research: Atmospheres*, **123 (10)**, 5188–5204, doi: 10.1029/2017JD026979.

Drushka, K., W. Asher, A. Jessup, E. Thompson, S. Iyer, and D. Clark, 2019a: Capturing fresh layers with the surface salinity profiler. *Oceanography*, **32**, doi: 10.5670/oceanog.2019.215.

Drushka, K., W. Asher, J. Sprintall, S. Gille, and C. Hoang, 2019b: Global patterns of submesoscale surface salinity variability. *Journal of Physical Oceanography*, **49**, 1669–1685, doi: 10.1175/JPO-D-19-0018.1.

Drushka, K., W. E. Asher, B. Ward, and K. Walesby, 2016: Understanding the formation and evolution of rain-formed fresh lenses at the ocean surface. *Journal of Geophysical Research: Oceans*, **121 (4)**, 2673–2689, doi: 10.1002/2015JC011527.

Fairall, C., E. Bradley, J. Godfrey, G. Wick, J. Edson, and G. Young, 1996b: Cool-skin and warm-layer effects on sea surface temperature. *Journal of Geophysical Research*, **101 (C1)**, 1295–1308, doi: 10.1029/95JC03190.

Fairall, C., E. Bradley, J. Hare, A. Grachev, and J. Edson, 2003: Bulk parameterization of air-sea fluxes for tropical ocean-global atmosphere coupled-ocean atmosphere response experiment. *Journal of Climate*, **16 (4)**, 571–591, doi: 10.1029/95JC03205.

Fairall, C., E. Bradley, D. Rogers, J. Edson, and G. Young, 1996: Bulk parameterization of air-sea fluxes for tropical ocean-global atmosphere coupled-ocean atmosphere response experiment. *Journal of Geophysical Research*, **101 (C2)**, 3747–3764, doi: 10.1029/95JC03205.

Feng, Z., S. Hagos, A. K. Rowe, C. D. Burleyson, M. N. Martini, and S. P. de Szoeke, 2015: Mechanisms of convective cloud organization by cold pools over tropical warm ocean during the AMIE/DYNAMO field campaign. *J. Adv. Model. Earth Syst.*, **7**, 357–381, doi: 10.1002/2014MS000384.

Gosnell, R., C. W. Fairall, and P. J. Webster, 1995: The sensible heat of rainfall in the tropical ocean. *Journal of Geophysical Research*, **100(C9) (18)**, 18 437–18 442, doi: 10.1029/95JC01833.

Gottschalck, J., P. Roundy, C. J. Schreck III, A. Vintzileos, and C. Zhang, 2013: Large-scale atmospheric and oceanic conditions during the 2011-12 DYNAMO field campaign. *Monthly Weather Review*, **141 (12)**, 4173–4196, doi: 10.1175/MWR-D-13-00022.1.

Gould, J., et al., 2004: Argo profiling floats bring new era of in situ ocean observations. *EOS Transactions, AGU*, **85 (19)**, 185–190, doi: 10.1029/2004EO190002.

Hackert, E. C., R. M. Kovich, A. J. Busalacchi, and J. Ballabrera-Poy, 2019: Impact of Aquarius and SMAP satellite sea surface salinity observations on coupled El Niño/Southern Oscillation forecasts. *Journal of Geophysical Research: Oceans*, **124 (7)**, 4546–4556, doi: 10.1029/2019JC015130.

Hagos, S., Z. Feng, K. Landu, and C. N. Long, 2014: Advection, moistening, and shallow-to-deep conection transitions during the initiation and propagation of Madden-Julian Oscillation. *J. Adv. Model. Earth Syst.*, **06**, doi: 10.1002/2014MS000335.

Hagos, S., Z. Feng, S. McFarlane, and L. Leung, 2013: Environment and the lifetime of tropical deep convection in a cloud-permitting regional model simulation. *Journal of the Atmospheric Sciences*, **70**, 2409–2425, doi: 10.1175/JAS-D-12-0260.1.

Halkides, D. J., D. E. Waliser, T. Lee, D. Menemenlis, and B. Guan, 2015: Quantifying the processes controlling intraseasonal mixed-layer temperature variability in the tropical Indian Ocean. *Journal of Geophysical Research: Oceans*, **120 (2)**, 692–715, doi: 10.1002/2014JC010139.

Hersbach, H., et al., 2020: The ERA5 global reanalysis. *Quarterly Journal of the Royal Meteorological Society*, **146 (730)**, 1999–2049, doi: 10.1002/qj.3803, `https://rmets.onlinelibrary.wiley.com/doi/pdf/10.1002/qj.3803`.

Hill, C., C. DeLuca, Balaji, M. Suarez, and A. Da Silva, 2004: The architecture of the earth system modeling framework. *Computing in Science & Engineering*, **6 (1)**, 18–28, doi: 10.1109/MCISE.2004.1255817.

Hogenegger, C. and B. Stevens, 2016: Coupled radiative convective equilibrium simlations with explicit and parameterized convection. *Journal of Advances in Modeling Earth Systems*, **8 (3)**, 1468–1482.

Holloway, C. E., A. A. Wing, S. Bony, C. Muller, H. Masunaga, T. S. L'Ecuyer, D. D. Turner, and P. Zuidema, 2017: Observing convective aggregation. *Surverys in Geophysics*, **38**, 1199–1236.

Hoskins, B. J. and D. J. Karoly, 1981: The steady linear response of a spherical atmosphere to thermal and orographic forcing. *Journal of Atmospheric Sciences*, **38 (6)**, 1179 – 1196, doi: 10.1175/1520-0469(1981)038<1179:TSLROA>2.0.CO;2.

Houze, R. A., 2004: Mesoscale convective systems. *Reviews of Geophysics*, **42**.

Hughes, K. G., J. M. Moum, and E. J. Shroyer, 2020: Evolution of the velocity structure in the diurnal warm layer. *J. of Phys. Oceanogr.*, **50**, 615–631, doi: 10.1175/JPO-D-19-0207.1.

Iacono, M. J., J. S. Delamere, E. J. Mlawer, M. W. Shephard, S. A. Clough, and W. D. Collins, 2008: Radiative forcing by long-lived greenhouse gases: Calculations with the AER radiative transfer models. *Journal of Geophysical Research: Atmospheres*, **113 (D13)**, doi: 10.1029/2008JD009944.

Iyer, S. and K. Drushka, 2021a: The influence of preexisting stratification and tropical rain modes on the mixed layer salinity response to rainfall. *JGR: Oceans*, doi: 10.1029/2021JC017574.

Iyer, S. and K. Drushka, 2021b: Turbulence within rain-formed fresh lenses during the SPURS-2 experiment. *J. Phys. Oceanogr., 51(5), 1705-1721*, **51 (5)**, 1705–1721, doi: 10.1175/JPO-D-20-0303.1.

Johnson, R. H., T. M. Rickenbach, S. A. Rutledge, P. E. Ciesielski, and W. H. Schubert, 1999: Trimodal characteristics of tropical convection. *Journal of Climate*, **12 (8)**, 2397 – 2418, doi: 10.1175/1520-0442(1999)012<2397:TCOTC>2.0.CO;2.

Kemball-Cook, S., B. Wang, and X. Fu, 2002: Simulation of the ISO in the ECHAM4 model: The impact of coupling with an ocean model. *Journal of Atmospheric Science*, **59 (9)**, 1433 – 1453, doi: 10.1175/1520-0469(2002)059<1433:SOTIOI>2.0.CO;2.

Kraus, E. and J. Turner, 1967: A one-dimensional model of the seasonal thermocline ii: The general theory and its consequences. *Tellus*, **19**, 98–106, doi: 10.1111/j.2153-3490.1967.tb01462.x.

Lambaerts, J., G. Lapeyre, R. Plougonven, and P. Klein, 2020: Atmospheric response to sea surface temperature mesoscale structures. *Journal of Geophysical Research: Atmospheres*, **118 (17)**, 9611–9621, doi: 10.1002/jgrd.50769.

Large, W. G., J. C. McWilliams, and S. C. Doney, 1994: Oceanic vertical mixing: A review and a model with a nonlocal boundary layer parameterization. *Reviews of Geophysics*, **32 (4)**, 363–403, doi: 10.1029/94RG01872.

Li, Y. and R. Carbone, 2012: Excitation of rainfall over the tropical western Pacific. *Journal of the Atmospheric Sciences*, **69 (10)**, 2983–2994, doi: 10.1175/JAS-D-11-0245.1.

Lindzen, R. S. and S. Nigam, 1987: On the role of sea surface temperature gradients in forcing low-level winds and convergence in the tropics. *Journal of Atmospheric Sciences*, **44 (17)**, 2418 – 2436, doi: 10.1175/1520-0469(1987)044<2418:OTROSS>2.0.CO;2.

Lucas-Picher, P., D. Argüeso, E. Brisson, Y. Tramblay, P. Berg, A. Lemonsu, S. Kotlarski, and C. Caillaud, 2021: Convection-permitting modeling with regional climate models: Latest developments and next steps. *WIREs Climate Change*, **12 (6)**, e731, doi: 10.1002/wcc.731.

Madden, R. A. and P. R. Julian, 1971: Detection of a 40–50 day oscillation in the zonal wind in the tropical Pacific. *Journal of Atmospheric Sciences*, **28 (5)**, 702 – 708, doi: 10.1175/1520-0469(1971)028<0702:DOADOI>2.0.CO;2.

Marshall, J., A. Adcroft, C. Hill, L. Perelman, and C. Heisey, 1997: A finite-volume, incompressible Navier Stokes model for studies of the ocean on parallel computers. *Journal of Geophysical Research: Oceans*, **102 (C3)**, 5753–5766, doi: 10.1029/96JC02775.

McPhaden, M. J., H. P. Freitag, S. P. Hayes, B. A. Taft, Z. Chen, and K. Wyrtki, 1988: The response of the equatorial Pacific Ocean to a westerly wind burst in May 1986. *Journal of Geophysical Research: Oceans*, **93 (C9)**, 10 589–10 603, doi: 10.1029/JC093iC09p10589.

Morrison, H., J. A. Curry, and V. I. Khvorostyanov, 2005: A new double-moment microphysics parameterization for application in cloud and climate models. part i: Description. *Journal of the Atmospheric Sciences*, **62 (6)**, 1665–1677, doi: 10.1175/JAS3446.1.

Moulin, A. J., J. N. Moum, E. L. Shroyer, and M. Hoecker-Martínez, 2021: Freshwater lens fronts propagating as buoyant gravity currents in the equatorial Indian Ocean. *Journal of Geophysical Research: Oceans*, **126 (8)**, doi: 10.1029/2021JC017186.

Moum, J. N., K. Pujiana, R.-C. Lien, and W. D. Smyth, 2016: Ocean feedback to pulses of the Madden–Julian Oscillation in the equatorial Indian Ocean. *Nature Communications*, **7 (13203)**, 1185–1199, doi: 10.1038/ncomms13203.

Moum, J. N., et al., 2014: Air–sea interactions from westerly wind bursts during the November 2011 MJO in the Indian Ocean. *Bulletin of the American Meteorological Society*, **95 (8)**, 1185–1199, doi: 10.1175/BAMS-D-12-00225.1.

Nakanishi, M. and H. Niino, 2009: Development of an improved turbulence closure model for the atmospheric boundary layer. *Journal of the Meteorological Society of Japan*, **87**, 895–912, doi: 10.2151/jmsj.87.895.

Paulson, C. and J. Simpson, 1977: Irradiance measurements in the upper ocean. *J. Phys. Oceanogr.*, **7 (6)**, 952–956, doi: 10.1175/1520-0485(1977)007<0952:IMITUO>2.0.CO;2.

Payne, R., 1972: Albedo of the sea surface. *J. Atmos. Sci.*, **28**, 959–970, doi: 10.1175/1520-0469(1972)029<0959:AOTSS>2.0.CO;2.

Pei, S., T. Shinoda, A. Soloviev, and R.-C. Lein, 2018: Upper ocean response to the atmospheric cold pools associated with the Madden-Julian Oscillation. *Geophysical Research Letters*, **45**, 5020–5029, doi: 10.1029/2018GL077825.

Pujiana, K., J. N. Moum, and W. D. Smyth, 2018: The role of turbulence in redistributing upper-ocean heat, freshwater, and momentum in response to the MJO in the equatorial Indian Ocean. *Journal of Physical Oceanography*, **48 (1)**, 197 – 220, doi: 10.1175/JPO-D-17-0146.1.

Reverdin, G., S. Morisset, J. Boutin, and N. Martin, 2012: Rain-induced variability of near sea-surface T and S from drifter data. *J. Geophys. Res.*, **117**, doi: 10.1029/2011JC007549.

Richenback, T. M. and S. A. Rutledge, 1998: Convection in TOGA COARE: Horizontal scale, morphology, and rainfall production. *Journal of the Atmospheric Sciences*, **55 (17)**, 2715–2729, doi: 10.1175/1520-0469(1998)055<2715:CITCHS>2.0.CO;2.

Riley Dellaripa, E. and E. Maloney, 2015: Analysis of MJO wind-flux feedbacks in the Indian Ocean using RAMA buoy observations. *Journal of the Meteorological Society of Japan. Ser. II*, **90**, 1–20, doi: 10.2151/jmsj.2015-021.

Ruddick, B., 1983: A practical indicator of the stability of the water column to double-diffusive activity. *Deep Sea Research Part A. Oceanographic Research Papers*, **30 (10)**, 1105–1107, doi: 10.1016/0198-0149(83)90063-8.

Rudnick, D. and R. Ferrari, 1999: Compensation of horizontal temperature and salinity gradients in the ocean mixed layer. *Science*, **283 (5401)**, 526–529, doi: 10.1126/science.283.5401.526.

Ruppert Jr., J. H. and R. H. Johnson, 2016: On the cumulus diurnal cycle over the tropical warm pool. *Journal of Advances in Modeling Earth Systems*, **08**, doi: 10.1002/2015MS000610.

Rydbeck, A. V., T. G. Jensen, and M. R. Igel, 2019: Idealized modeling of the atmospheric boundary layer response to SST forcing in the Western Indian Ocean. *Journal of the Atmospheric Sciences*, **76 (7)**, 2023–2042, doi: 10.1175/JAS-D-18-0303.1.

S., M., T. P., M. G., L. J.-J., Y. T., and T. K., 2012: Impact of intra-daily SST variability on ENSO characteristics in a coupled model. *Climate Dynamics*, **39**, 681–707, doi: 10.1007/s00382-011-1247-2.

Shackelford, K., C. A. DeMott, P. J. van Leeuwen, E. Thompson, and S. Hagos, 2022: Rain-induced stratification of the equatorial Indian Ocean and its potential feedback to the atmosphere. *Journal of Geophysical Research: Oceans*, **127 (3)**, e2021JC018 025, doi: 10.1029/2021JC018025.

Skamarock, W. C., et al., 2019: A description of the advanced research WRF version 4. *NCAR Tech. Note NCAR/TN-556+STR*, 145 pp., doi: 10.5065/1dfh-6p97.

Skyllingstad, E. D., S. P. de Szoeke, and L. W. O'Neill, 2019: Modeling the transient response of tropical convection to mesoscale SST variations. *Journal of the Atmopsheric Sciences*, **76 (5)**, 1227–1244.

Soloviev, A. and R. Lukas, 1997: Observation of large diurnal warming events in the near-surface layer of the western equatorial Pacific warm pool. *Deep Sea Research Part I: Oceanographic Research Papers*, **44 (6)**, 1055–1076, doi: 10.1016/S0967-0637(96)00124-0.

Soloviev, A., S. Matt, and A. Fujimura, 2015: Three-dimensional dynamics of fresh water lenses in the ocean's near-surface layer. *Oceanography*, **28 (1)**, 142–149, doi: 10.5670/oceanog.2015.14.

Stuart-Menteth, A. C., I. S. Robinson, and P. G. Challenor, 2003: A global study of diurnal warming using satellite-derived sea surface temperature. *Journal of Geophysical Research: Oceans*, **108 (C5)**, 3155, doi: 10.1029/2002JC001534.

Sui, C. H., K. M. Lau, T. Y. M., and S. D. A., 1997: Diurnal variations in tropical oceanic cumulus convection during TOGA COARE. *Journal of the Atmospheric Sciences*, **54 (5)**, 639–655, doi: 10.1175/1520-0469(1997)054<0639:DVITOC>2.0.CO;2.

Sun, R., A. C. Subramanian, B. D. Cornuelle, M. R. Mazloff, A. J. Miller, F. M. Ralph, H. Seo, and I. Hoteit, 2021: The role of air–sea interactions in atmospheric rivers: Case studies using the SKRIPS regional coupled model. *Journal of Geophysical Research: Atmospheres*, **126 (6)**, e2020JD032 885, doi: 10.1029/2020JD032885, e2020JD032885 2020JD032885, `https://agupubs.onlinelibrary.wiley.com/doi/pdf/10.1029/2020JD032885`.

Sun, R., A. C. Subramanian, A. J. Miller, M. R. Mazloff, I. Hoteit, and B. D. Cornuelle, 2019: SKRIPS v1.0: a regional coupled ocean–atmosphere modeling framework (MITgcm–WRF) using ESMF/NUOPC, description and preliminary results for the Red Sea. *Geoscientific Model Development*, **12 (10)**, 4221–4244, doi: 10.5194/gmd-12-4221-2019.

Terray, P., K. Kamala, S. Masson, G. Madec, A. Sahai, J.-J. Luo, and T. Yamagata, 2012: The role of the intra-daily SST variability in the indian monsoon variability and monsoon-ENSO–IOD relationships in a global coupled model. *Climate Dynamics*, **39**, 729–754, doi: 10.1007/s00382-011-1240-9.

Thompson, E. J., J. N. Moum, C. W. Fairall, and S. A. Rutledge, 2019: Wind limits on rain layers and diurnal warm layers. *Journal of Geophysical Research: Oceans*, **124**, doi: 10.1029/2018JC014130.

Vinogradova, N., et al., 2019: Satellite salinity observing system: Recent discoveries and the way forward. *Frontiers in Marine Science*, doi: 10.3389/fmars.2019.00243.

Watson, A. J., U. Schuster, J. D. Shutler, T. Holding, I. G. C. Ashton, P. Landschützer, D. K. Woolf, and L. Goddijn-Murphy, 2020: Revised estimates of ocean-atmosphere CO2 flux are consistent with ocean carbon inventory. *Nat Commun*, **11**, doi: 10.1038/s41467-020-18203-3.

Webster, P. J., C. A. Clayson, and J. A. Curry, 1996: Clouds, radiation, and the diurnal cycle of sea surface temperature in the tropical western Pacific. *Journal of Climate*, **9 (8)**, 1712 – 1730, doi: 10.1175/1520-0442(1996)009<1712:CRATDC>2.0.CO;2.

Weickmann, K. M., 1983: Intraseasonal circulation and outgoing longwave radiation modes during northern hemisphere winter. *Monthly Weather Review*, **111**, 1838–1858., doi: 10.1175/1520-0493(1983)111<1838:ICAOLR>2.0.CO;2.

Wijesekera, H. W., C. A. Paulson, and A. Huyer, 1999: The effect of rainfall on the surface layer during a westerly wind burst in the western equatorial Pacific. *Journal of Physical Oceanography*, **29 (4)**, 612 – 632, doi: 10.1175/1520-0485(1999)029<0612:TEOROT>2.0.CO;2.

Wing, A. A., K. Emanuel, C. E. Holloway, and C. Muller, 2017: Convective self-aggregation in numerical simulations: A review. *Surverys in Geophysics*, **38**, 1173–1197.

Woolnough, S., F. Vitart, and M. A. Balmaseda, 2007: The role of the ocean in the Madden-Julian Oscillation: Implications for MJO prediction. *Quarterly Journal of the Royal Meteorological Society*, **133**, 117–128, doi: 10.1175/1520-0485(1999)029<0612:TEOROT>2.0.CO;2.

Yokoi, S., M. Katsumata, and K. Yoneyama, 2014: Variability in surface meteorology and air-sea fluxes due to cumulus convective systems observed during CINDY/DYNAMO. *Journal of Geophysical Research: Atmospheres*, **119 (5)**, 2064–2078, doi: 10.1002/2013JD020621.

Yoneyama, K., C. Zhang, and C. Long, 2013: Tracking pulses of the Madden-Julian Oscillation. *Bulletin of the American Meteorological Society*, **94 (12)**, 1871–1891, doi: 10.1175/BAMS-D-12-00157.1.

Zhang, C. and S. P. Anderson, 2003: Sensitivity of intraseasonal perturbations in SST to the structure of the MJO. *Journal of the Atmospheric Sciences*, **60 (17)**, 2196 – 2207, doi: 10.1175/1520-0469(2003)060<2196:SOIPIS>2.0.CO;2.

Zhang, C., M. Dong, S. Gualdi, H. H. Hendon, E. D. Maloney, A. Marshall, K. R. Sperber, and W. Wang, 2006: Simulations of the Madden-Julian oscillation in four pairs of coupled and uncoupled global models. *Climate Dynamics*, **27 (17)**, 573 – 592, doi: 10.1007/s00382-006-0148-2.

Zhao, N. and T. Nasuno, 2020: How does the air-sea coupling frequency affect convection during the MJO passage? *Journal of Advances in Modeling Earth Systems*, **12**, doi: 10.1029/2020MS002058.

Zuidema, P., G. Torri, C. Muller, and A. Chandra, 2017: A survey of precipitation-induced atmospheric cold pools over oceans and their interactions with the larger-scale environment. *Surveys in Geophysics*, **38**, 1283–1305, doi: 10.1007/s10712-017-9447-x.